THE MATERHORN
Unraveling the Intricacies of Mountain Weather

by H. J. S. Fernando, E. R. Pardyjak, S. Di Sabatino, F. K. Chow, S. F. J. De Wekker, S. W. Hoch, J. Hacker, J. C. Pace, T. Pratt, Z. Pu, W. J. Steenburgh, C. D. Whiteman, Y. Wang, D. Zajic, B. Balsley,* R. Dimitrova, G. D. Emmitt, C. W. Higgins, J. C. R. Hunt, J. C. Knievel, D. Lawrence, Y. Liu, D. F. Nadeau, E. Kit, B. W. Blomquist, P. Conry, R. S. Coppersmith, E. Creegan, M. Felton, A. Grachev, N. Gunawardena, C. Hang, C. M. Hocut, G. Huynh, M. E. Jeglum, D. Jensen, V. Kulandaivelu, M. Lehner, L. S. Leo, D. Liberzon, J. D. Massey, K. McEnerney, S. Pal, T. Price, M. Sghiatti, Z. Silver, M. Thompson, H. Zhang, and T. Zsedrovits

Comprehensive, multiscale, and multidisciplinary observations allow scientists to discover novel flow physics, address current deficiencies of predictive models, and improve weather prediction in mountainous terrain.

Through woods and mountain passes
the winds, like anthems, roll.
—Henry Wadsworth Longfellow

For centuries, humans have been both fascinated and awed by mountain weather, and its intriguing aberrancy continues to baffle weather forecasters. For instance, a clear morning on a tranquil mountain slope can swiftly change into violent storms within hours while a nearby valley remains calm. The variability of mountain weather spans a wide swath of space–time scales, contributing to a myriad of phenomena that stymie the predictability of mountain weather. Although isolated mountains are rare, about 20% of Earth's land surface is covered by mountainous areas (Louis 1975). Topography less than 600 m in height (<5% of the atmospheric-scale height) is referred to as hills, but demarcations between different topographic features remain ambiguous. Orographic mosaics that incorporate slopes, valleys, canyons, escarpments, gullies, and buttes (also known as complex terrain) cover about 70% of Earth's land surface (Strobach 1991). The majority of the world's urban areas have emerged in complex terrain because of

accompanying water resources. Systematic studies of mountain weather date back to the 1850s, followed by a decline of scientific activity in the early 1900s owing to observational difficulties. A resurgence of research occurred in the midtwentieth century with the advent of aerological networks (Bjerknes et al. 1934) as well as groundbreaking advances of mountain-wave and slope-flow studies (Prandtl 1942; Queney 1948; Long 1953). Vivid applications in areas of urban air pollution (Ellis et al. 2000; Fernando and Weil 2010), dispersion in cities (Allwine et al. 2002), wind energy harvesting (Banta et al. 2013), aviation (Politovich et al. 2011), alpine warfare (Winters et al. 2001), and firefighting (Albini et al. 1982) have burgeoned mountain meteorology, but understanding of flow physics and fidelity of predictions leaves much to be desired. Reviews of relevant past research are found in Taylor et al. (1987), Blumen (1990), Baines (1998), Belcher and Hunt (1998), Whiteman (2000), Wood (2000), Barry (2008), Fernando (2010), and Chow et al. (2013).

Prompted by applications-driven overarching science questions, in 2011 the U.S. Department of Defense (DoD) funded a 5-yr Multidisciplinary University Research Initiative (MURI) aimed at

improving weather prediction in mountainous terrain. Dubbed MATERHORN, this effort involves 11 principal investigators from five academic institutions (see sidebar on "Program synopsis"). Ten additional collaborators have joined the project with an array of research tools [more information can be found online (http://dx.doi.org/10.1175/BAMS-D-12-00023.2) in the supplementary information]. At the outset, the existing barriers to mountain weather forecasting were reviewed and critical science and modeling needs were identified, and based on which, a multifaceted research effort was developed. Commensurate with available resources, the focus was limited to arid/semiarid regions and scales at or smaller than the mesoscale, thus deemphasizing issues such as orographic precipitation and marine pushes. Two extensive field campaigns were conducted within the first 3 years, and their design drew guidance from recent complex-terrain field campaigns such as Vertical Transport and Mixing (VTMX; Doran et al. 2002), Mesoscale Alpine Programme (MAP; Rotach and Zardi 2007), Meteor Crater Experiment (METCRAX; Whiteman et al. 2008), Terrain-Induced Rotor Experiment (T-REX; Grubišić et al. 2008), the Phoenix Air Flow Experiment (PAFEX; Pardyjak et al. 2009), Cold-Air Pooling Experiment (COLPEX; Price et al. 2011), Phoenix Evening Transition Flow Experiment (TRANSFLEX; Fernando et al. 2013), Boundary-Layer Late Afternoon and Sunset Turbulence (BLLAST; Lothon et al. 2014), and Meteo-diffusion (Leo et al. 2015a).

The Granite Mountain Atmospheric Science Testbed of the U.S. Army Dugway Proving Ground (DPG) was selected as the field site. This site has the advantages of a large spatial extent, richness in mountain weather phenomena, interesting climatological regimes, distinct (but few) land-use types, an existing instrumentation network, and unique logistical support. A repertoire of measurement tools were used to observe processes over a wide range of space–time scales, which was augmented by model evaluations and improvements. This paper presents an overview of MATERHORN, starting with an outline of complex-terrain flow processes followed by discussions of critical science gaps, field campaigns, modeling efforts, and preliminary results.

FLOW PROCESSES IN COMPLEX TERRAIN.

Figure 1 schematizes mountain-valley flow processes over a DPG topographic map. Under weak synoptic (wind speed $U_s > 5$ m s^{-1}) conditions dominated by high pressure, the characteristic winds are downslope (katabatic) and downvalley at night (blue arrows) while upslope (anabatic) and upvalley during the day (red), signifying thermal circulation (Whiteman 2000; Fernando 2010; Zardi and Whiteman 2013). Pure slope and valley winds are rare in nature, since they interact among themselves and with synoptic flow. At night, downslope/downvalley winds drain through gaps and canyons (Mayr et al. 2007), separate out from the slopes as intrusions (Lu and Turco 1994), interact with smaller topographic features (Baines 1998), and, as will be discussed later, collide with each other to create spasmodic turbulence episodes. Colder nocturnal air draining down from the slopes accumulates in confined valleys, forming stable cold pools that are weakly turbulent (Whiteman et al. 2008; Monti et al. 2002). Pulsations of katabatic flow at critical internal-wave frequency (Princevac et al. 2008), interleaving intrusions arriving

AFFILIATIONS: Fernando, Di Sabatino, Pratt, Dimitrova, Hunt, Conry, Coppersmith, Hocut, Leo, Liberzon, McEnerney, Silver, Thompson, and Zsedrovits—University of Notre Dame, Notre Dame, Indiana; Pardyjak, Hoch, Pu, Steenburgh, Whiteman, Gunawardena, Hang, Jeglum, Jensen, Kulandaivelu, Lehner, Massey, Price, and Zhang—University of Utah, Salt Lake City, Utah; Chow—University of California, Berkeley, Berkeley, California; De Wekker, Pal, and Sghiatti—University of Virginia, Charlottesville, Virginia; Hacker—Naval Postgraduate School, Monterey, California, and National Center for Atmospheric Research, Boulder, Colorado; Pace and Zajic—U.S. Army Dugway Proving Ground, Utah; Wang, Creegan, Felton, and Huynh—U.S. Army Research Laboratory, Adelphi, Maryland; Balsley and Lawrence—University of Colorado Boulder, Boulder, Colorado; Emmitt—Simpson Weather Associates, Charlottesville, Virginia; Higgins—Oregon State University, Corvallis, Oregon; Knievel and Liu—National Center for Atmospheric Research, Boulder, Colorado; Nadeau—École Polytechnique de Montréal, Montreal, Quebec, Canada; Kit—University of Notre Dame, Notre Dame, Indiana, and Tel Aviv University, Tel Aviv, Israel; Blomquist and Grachev—University of Notre Dame, Notre Dame, Indiana, and National Oceanic and Atmospheric Administration, Silver Spring, Maryland, and University of Colorado Boulder, Boulder, Colorado
* In memoriam.

CORRESPONDING AUTHOR: Harindra Joseph Fernando, Environmental Fluid Dynamics Laboratories, Department of Civil and Environmental Engineering and Earth Sciences and Department of Aerospace and Mechanical Engineering, 156 Fitzpatrick Hall, University of Notre Dame, Notre Dame, IN 46556-5637
E-mail: hfernand@nd.edu

The Mountain Terrain Atmospheric Modeling and Observations (MATERHORN) Program was designed to investigate complex-terrain meteorology over a wide range of scales, topographic features, and driving mechanisms by drawing expertise from multiple disciplines and by employing complementary research methodologies. The principal participants are the University of Notre Dame (UND; lead); University of California, Berkeley (UCB); Naval Postgraduate School (NPS); University of Utah (UU); and University of Virginia (UVA).

MATERHORN consists of four components working symbiotically:

• The modeling component (MATERHORN-M) investigates predictability at the mesoscale, in particular, sensitivity (error growth) to initial conditions at various lead times, dependence on boundary conditions and input background properties, as well as merits of different data-assimilation techniques. It also attempts high-resolution simulations with novel modeling and terrain-representation methodologies.

• The experimental component (MATERHORN-X) mainly conducts field measurements at unprecedented spatiotemporal detail by deploying arrays of routine, high-end, and newly developed instrumentation. Laboratory experiments are used for process studies.

• The technology development component (MATERHORN-T) enables currently untenable meteorological observations. The developments include an instrumented UAV, sensors for moisture and fog measurements, and a combined hot-film/sonic anemometer system for probing turbulence down to Kolmogorov scales. Advanced data retrieval and processing algorithms are also attempted.

• The parameterization component (MATERHORN-P) develops high-fidelity physics-based fundamental (quantitative) relationships for complex-terrain processes, which are implemented in mesoscale models followed by model evaluations.

from different topographies (Fernando et al. 2013), and shear layers of flow fanning out from the gaps all contribute to the weakly turbulent state. This differs from very stable boundary layers over flat terrain, where turbulence is highly intermittent in space and time (Mahrt 1999).

As the nocturnal stable boundary layer (SBL) breaks down during the morning transition, paving the way for a daytime convective boundary layer (CBL), a flow reversal occurs from downslope/downvalley to upslope/upvalley. Upslope flow may separate on the slopes in the form of thermal plumes, topped by cumulus clouds (Banta 1984; Hocut et al. 2015). During the evening transition, the signs of heat flux and vertical temperature gradient reverse, convective turbulence collapses, and the downslope/downvalley flow system reemerges. A host of physical processes contribute to morning (Whiteman 1982; Princevac and Fernando 2008) and evening transitions (Hunt et al. 2003; Nadeau et al. 2011). Other flow types include local (micro) circulations driven by thermal and roughness contrasts arising from land-cover inhomogeneities (Jannuzzi 1993; Rife et al. 2002).

Under strong synoptic conditions ($U_s \gg U_t$, where U_t is the characteristic velocity of the thermal circulation), flow is energetic and inertially dominated. When the approach flow is stably stratified (with velocity U and buoyancy frequency N), it responds to the topography (height h) by distorting the flow over horizontal spatial scales on the order of the Rossby deformation radius (Hunt et al. 2004). Ensuing local phenomena are dependent on the Froude number (Fr = U/Nh), with thermal circulation becoming insignificant when Fr > 0.5

(Poulos et al. 2000). Stably stratified mountain wakes consist of lee waves, propagating internal waves, rotors, separated flow, and intriguing vortex structures (Long 1972; Lin et al. 1992; Hunt et al. 2006). If the topography is 3D, the flow above the dividing streamline goes over the mountain while the rest flows around the mountain (Snyder et al. 1985). In 2D cases, the flow below the dividing streamline is blocked upstream, but when there is a gap in the topography the flow can leak through it, depending on Fr and the gap aspect ratio (Baines 1979). At very high Fr, the flow is similar to the neutral case, with shear-layer separation and vortex shedding at the edges of the topography (Brighton 1978).

Daytime heating leads to the CBL development, and when the synoptic condition is such that U_s is of the same order as the Deardorff (1970) convective-scale w_*, the upslope flow on the windward side is reinforced while that on the leeward side is weakened and separated to form recirculation cells (Fernando 2010). Numerical predictions under strong synoptic conditions ($U_s \gg U_t \sim w_*$) tend to be better than those under thermal circulation conditions, but, in general, both could be desired for near-surface predictions (Fernando and Weil 2010). The complexities associated with interacting wakes and shear layers of neighboring mountains, canyon effects, gap flows, and microcirculations are only beginning to be investigated.

CRITICAL SCIENCE NEEDS. Preceding MATERHORN, a workshop entitled "Overcoming Scientific Barriers to Weather Support in Mountainous Terrain" was held in Tempe, Arizona, 1–2 February

2010. Twenty-six invitees representing academia and stakeholders compiled a list of research needs, barriers, and experiences (a report is available from the corresponding author), a subset of which was selected for investigations:

1) the predictability of near-surface wind and temperature in complex terrain remains poor, in part owing to meager understanding of near-surface processes;

2) surface-layer predictions are sensitive to soil moisture and soil properties, which are inputs to the models, yet these key parameters are not accurately measured in field studies to quantify their role;

3) mesoscale models are more prone to forecast error when predicting in complex terrain than over flat terrain, possibly because of the large number of processes exclusive to complex terrain in the subgrid scales;

4) proper assimilation of near-surface observations is useful for improving short-range forecasts;

5) coordinated high-resolution observations from meso- to dissipation scales are needed using dense instrumentation networks, possibly using novel instrumentation, as most past observations have focused on a limited ranges of scales;

6) turbulence closure models and boundary layer parameterizations need to be revisited to help develop better subgrid parameterizations, particularly for the SBL; and

7) there is potential for ultra-high-resolution (<50-m horizontal) simulations using techniques such as the immersed boundary method (IBM).

Considering 1–7, MATERHORN was focused on high-resolution observations, near-surface processes,
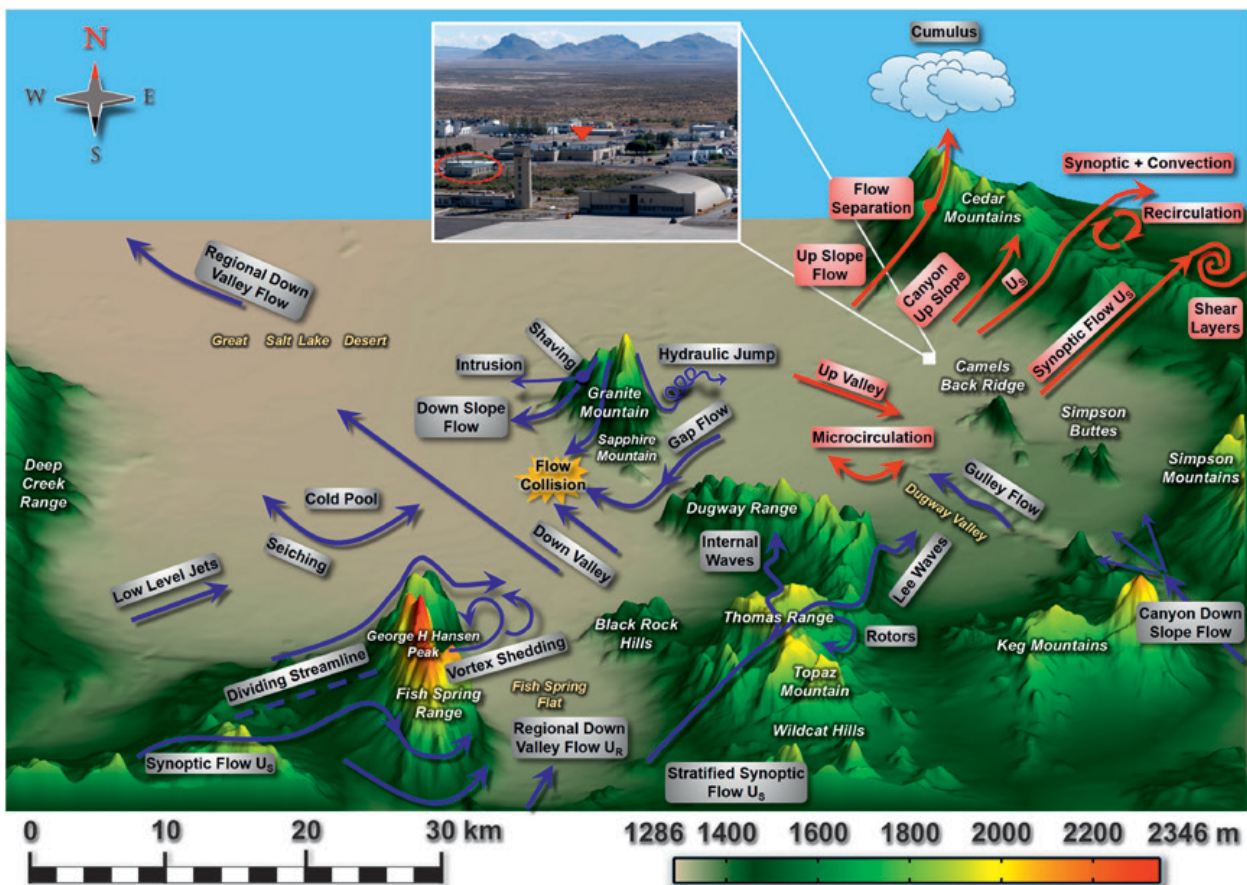

FIG. 1. Physical processes in complex terrain, illustrated on a topographic map of the DPG domain. The spatial and the elevation (shading) scales are shown below. Blue arrows represent nocturnal flows; red arrows represent daytime flows. An arbitrary direction has been used for illustration of synoptic effects (which typically varies from northwest to north to northeast in DPG). Shown in the inset are the control center (red arrow) and Ditto meteorological building (circled) of GMAST.

the role of surface and upper-soil-layer properties, boundary layer parameterizations, data assimilation, and high-resolution (large eddy) simulations (LESs) within mesoscale models.

MATERHORN-X. Two major field campaigns were conducted with high-resolution measurements, focusing on conditions dominated by thermal circulations and strong synoptic forcing. Another smaller study focused on fog formation, which will be a topic of future publications. The field site, equipment, and execution of the first two experiments are discussed next.

Field site. The Granite Mountain Atmospheric Science Testbed (GMAST) is a part of the U.S. Army DPG shown in Fig. 1. DPG is located 137 km southwest of Salt Lake City, Utah, and consists of 3700 km² of land in complex terrain with two dominant land-use types: playa and desert shrub. The region is dry with annual precipitation of 197 mm yr⁻¹ (WRCC 2014). Within the DPG is a nominally isolated topographic feature, Granite Mountain (GM), 11.8 km in length, 6.1 km at its widest, and peak elevation 0.84 km above the valley floor, which itself is 1.3 km above mean sea level (MSL). The surroundings of the GM are well instrumented for providing meteorological support for weapon systems testing, thus forming GMAST. With DoD-controlled roads, air space, and facilities, it was possible to operate unmanned aerial vehicles (UAV), low-flying manned aircraft, and large smoke-release apparatuses. A special agreement between UND, UU, and DPG allowed access to this highly secured DoD facility on the premise that DPG would also benefit from the findings to improve its own meteorological capabilities. The fall campaign period (25 September–31 October 2012) was characterized by quiescent, dry, fair weather ($U_s < 5$ m s⁻¹) periods dominated by thermal circulation and the spring campaign (1–31 May 2013) by synoptic forcing. A dry experimental run (25–30 August 2012) helped fine-tune the instrument placement and logistics.

Instrumentation and observing locations. The GMAST core (basic) instrumentation consisted of 31 surface atmospheric measurement systems (SAMS), 51 mini-SAMS, and over 100 portable weather instrumentation data systems (PWIDS). SAMS and mini-SAMS are 10-m towers with vane anemometers (RM Young model 05103) at 2 and 10 m above ground level (AGL) to measure wind speed and direction and the temperature T and relative humidity (RH) at 2 m (Fig. 2). They both measure surface pressure and solar radiation, the

difference being that mini-SAMS have additional T and RH sensors at 10 m while SAMS measure precipitation and soil temperature. PWIDS are 2-m portable masts on tripods, with a wind monitor and T–RH probes at 2 m. All data from the core instrumentation are transmitted wirelessly to the DPG Meteorology Division (Fig. 1) via a spread spectrum radio.

The core infrastructure was augmented with an extensive suite of investigator-provided and DPG/National Oceanic and Atmospheric Administration (NOAA)/National Center for Atmospheric Research (NCAR)-loaned instrumentation concentrated at six intensive observing sites (IOS; Fig. 3), selected based on science plans and logistical constraints:

A: IOS-Playa was in the Great Salt Lake Desert west of GM; the area is extremely flat, smooth, and mostly devoid of vegetation, with a thin crust of crystalline salt above layers of alkaline sediments (Boettinger 2009). It is characterized by high albedo, low roughness length (see Table ES1), and seasonally changing moisture and albedo (Hang et al. 2015, manuscript submitted to *Bound.-Layer Meteor.*). Studies on the surface energy budget, internal waves, finescale turbulence, skin flows, and the effects of contrasting albedo, roughness, and moisture availability were conducted therein.

B: IOS-Obverse was the footprint where north/northwesterly/northeasterly approach flow impinges on the GM, yielding a range of phenomena such as dividing streamlines, vortex shedding, and wake flows.

C: IOS-WS (west slope) was on the western slope of GM for studies on slope flows and their interaction with synoptic, valley, and canyon flows.

D: IOS-Gap was a flow exchange area covered by sparse desert shrub vegetation between west and east basins. This site covered a small gap and a big gap. (The nominally semienclosed area east of the GM is referred to as the east basin, and the similar confinement to the west of GM is the west basin.)

E: IOS-ES (east slope) was on the eastern slope of GM. Covered by sparse desert shrub vegetation and long grasses, local slope flows played an important role at this site, including flow collisions, critical internal-wave oscillations, and seiching motions.

F: IOS-Sagebrush was located east of the GM and centrally in the main valley. Covered by sparse desert shrub vegetation, it was highly representative of the land cover in DPG. This site was in the
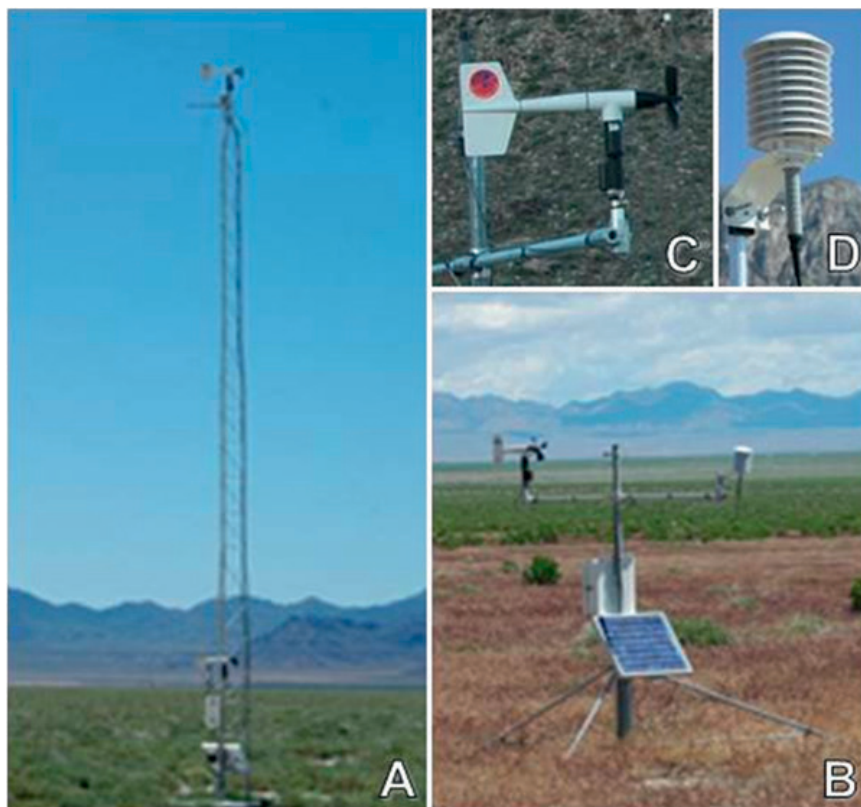
Fig. 2. GMAST core instrumentation: (a) SAMS/mini-Sams, (b) PWIDs, (c) vane anemometer, and (d) HMP45 temperature–relative humidity probe in radiation shield.

multiple levels of subsurface temperature. Sonic anemometers were also placed at 0.5 m AGL to investigate skin flows, a known phenomenon (Clements et al. 2003) yet unresolved by both numerical models and observations.

The IOS-ES had five heavily instrumented towers [ES-1–ES-5 (see Fig. 3), with ES5 at the foothill], with a total of 30 sonics, Krypton hygrometers, or LI-COR infrared gas analyzers (for eddy covariance, CO_2, water vapor fluxes), 9 HOBO temperature dataloggers, 13 local energy-balance measurement stations (LEMS), and lidars with hemispherical scanners. At times, three lidars were used for virtual tower mode operations (Y. Wang et al. 2014, unpublished manuscript) and on other occasions IOS-ES

path of the nocturnal mesoscale drainage flows over the Dugway Valley and at times was influenced by slope flows from different directions.

The placement of auxiliary instrumentation in IOS was guided by physical intuition and mesoscale model (hindcasting) runs. Photographs of auxiliary instrumentation are shown in Fig. 4, and their specifications are in Table ES2. All IOSs had instrumented towers, at least one 20 m in height, along with a suite of other sensors. Some instruments were relocated and additional instrumentation was brought in periodically as deemed necessary. The towers measured some or all of the following: 1) T, RH, wind velocities, momentum, and sensible heat fluxes (using 3D sonics and fine-wire thermocouples, located at 2, 5, 10, and 20 m and operating at 20 Hz); 2) CO_2 and water vapor concentration (open-path infrared gas analyzers) and fine-structure temperature profiles (~25 thermocouples up to 10 m, with enhanced vertical resolution near the ground); 3) full radiation budget (incoming and outgoing long- and shortwave fluxes at 2–3 m); 4) infrared (IR) surface temperature; and 5) soil heat flux, soil moisture, soil thermal properties, as well as

had tethered-balloon profiling. A fiber optic distributed temperature sensing (DTS) system measured the temperature variation along a 2-km track of the slope at 0.5 and 2 m AGL. The DTS uses the Raman scattering principle for laser light confined within a fiber optic cable to determine the spatially resolved temperature of the cable (Thomas et al. 2012). IOS-ES also housed fine-resolution combo probes developed by MATERHORN-T, an extension of a prototype developed at NCAR. It consisted of in situ calibrated 3D hot films collocated with 3D sonic anemometers that measured turbulence down to Kolmogorov dissipation scales (Kit et al. 2010). A FLIR IR camera facing uphill measured the spatiotemporal distribution of the surface IR temperatures. Smoke releases illuminated by a powerful argon–ion laser as well as by natural light portrayed large-scale flow structures and processes.

The IOS-WS consisted of two towers (WS-1 and WS-2), a SAMS station, eight HOBOs, and a LEMS along the western slope of GM for observing the interactions of synoptic and slope flows as well as contrasting developments of thermal circulations on the east and west slopes. WS-1 and the LEMS were
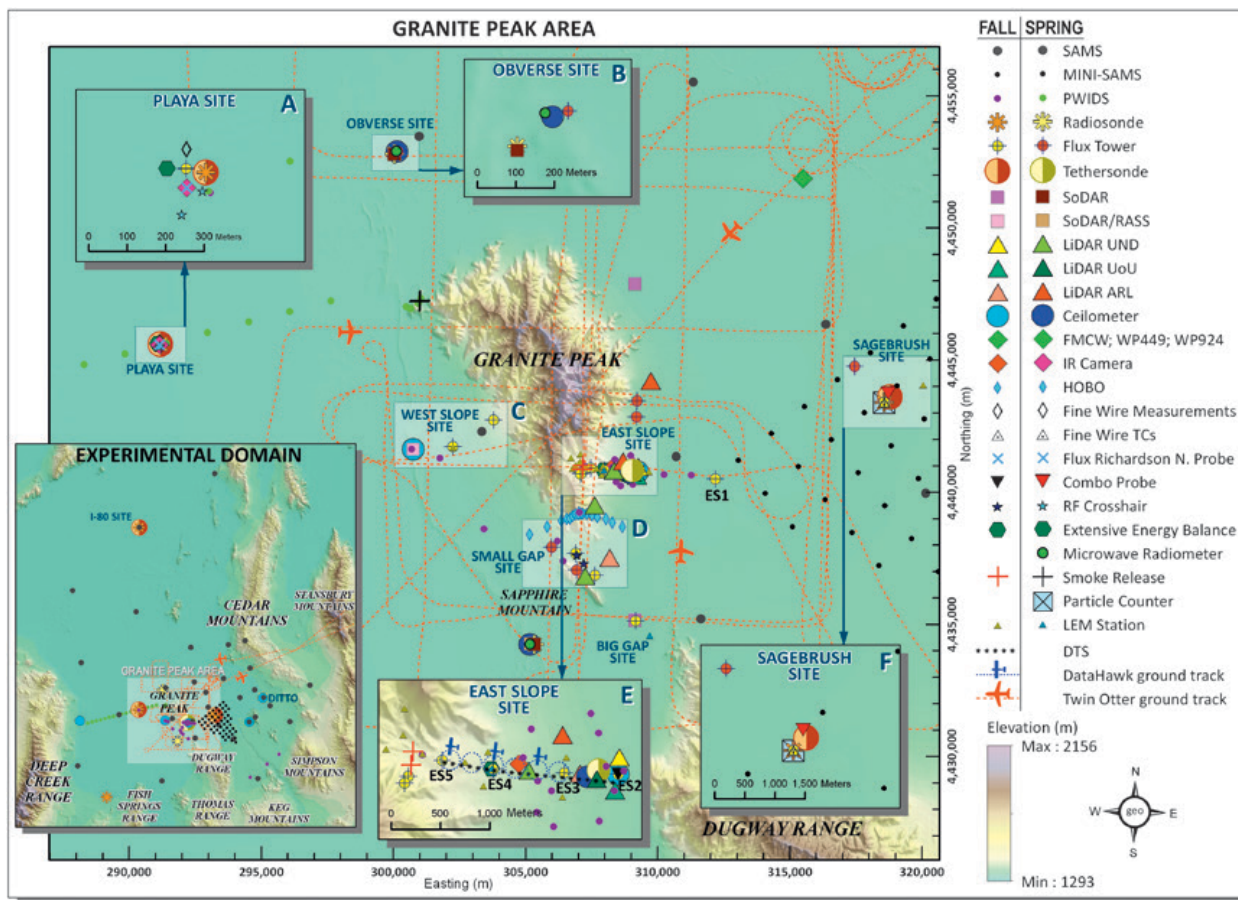
Fig. 3. Instrument placement during fall and spring campaigns. Insets provide details of IOSs as well as the full experimental domain (bottom-left inset). Only the additional instruments deployed (or relocated) for the spring experiment are shown under the "spring" column (courtesy of Dott. Ing. Roberto Perrone).

on the lower portion of the slope approximately 20 m above the Playa floor. The former was a 28-m tower instrumented with six levels of 3D sonics and *T*–RH sensors. During the fall campaign, IOS-WS hosted a sound detection and range/radio acoustic sounding system (SoDAR/RASS), a ceilometer, and additional PWIDS. The 20-m WS-2 was located farther along the slope with five sonics, a vane anemometer, Krypton hygrometer, 12 thermocouples, and extensive surface energy budget instrumentation.

The IOS-Sagebrush had a 20-m tower equipped with sonics, Campbell infrared gas analyzers, energy-balance equipment, and fine-wire thermocouples. Tethered-balloon soundings were operated at this site synchronous with the Playa sites. Upper-air (radiosonde) soundings were also launched at this site. Additional towers in the spring campaign included a 10-m mast approximately 2 km northwest of the main site with two 3D hot-film combos at two different heights and a 28-m tower with sonics and *T*–RH sensors at five heights.

The IOS-Playa featured unique instrumentation for finescale turbulence, employing a near-surface flux Richardson number (hot wire) probe, complementing the ES-2/Sagebrush combos. Also at IOS-Playa were a high-resolution thermal image velocimetry system (for near-surface temperature and velocity fluctuations), tethered-balloon and radiosonde sounding systems, and a heavily instrumented 20-m tower. In the spring, this site hosted two MATERHORN-T developed radio frequency (RF) measurement systems called RF polarimetric crosshairs. They characterized polarization signatures of signals on a receiving antenna, thus allowing the measurement of the electromagnetic response of emitted polarized radiation caused by environmental changes (Pratt et al. 2014). This instrument measured surface moisture at approximately 1-km scale (i.e., mesoscale grid resolution). For both campaigns, a RF-crosshairs system was deployed at the IOS-Gap. Manual soil moisture observations were also conducted at IOS-Playa during the spring campaign

to characterize soil moisture spatial variability and its role on the energy balance and land–atmosphere moisture exchange (Hang et al. 2015, manuscript submitted to *Bound.-Layer Meteor.*).

The instrumentation at IOS-Gap was suitably distributed over small and large gaps southeast of the GM, at the top of Sapphire Mountain as well as at multiple locations in the proximity. During the spring, a mini-SoDAR, microwave radiometer profiler (MWRP; for vertical profiles of temperature, liquid water content, and humidity up to 10 km), ceilometer, and radiosonde launches were deployed approximately 2.5 km southwest of Sapphire Mountain.

The IOS-Obverse provided approach flow information for the spring campaign, based on a 32-m tower located 400 m northwest of GM with 3D sonics collocated with T–RH sensors (2, 4, 6, 8, 16, and 28 m) and an open path CO_2–H_2O analyzer (LiCOR, 28 m). Also included were a MWRP, ceilometer, mini-SoDAR, and frequency-modulated continuous-wave (FM-CW) radar (Eaton et al. 1995) for profiling background thermodynamic structure. PWIDS recorded the local flow close to the GM leading edge. A scanning lidar and three towers along the east side of GM captured the leeside separated flow. At least eight upwind radiosonde launches per intensive observing period (IOP) provided information for data-assimilation studies. Elaborate multiple smoke releases provided information on flow physics related to dividing streamlines, streak lines, and flow separation (Leo et al. 2015b, manuscript submitted to *Bound.-Layer Meteor.*).

Aerial measurements were performed by the (manned) NPS Twin Otter Aircraft with Doppler Wind Lidar (TODWL) as well as unmanned aerial vehicles (UAV) dubbed DataHawk and ND-Flamingo. In the fall campaign, TODWL flights crisscrossed the basin at 2400 m AGL, transecting the GM ridge, while conically scanning the terrain with onboard Doppler lidar to probe the mountain flows (De Wekker et al. 2012). Seven TODWL flights were conducted during IOPs 4–7, collecting data during four afternoons and three mornings. DataHawk flights flew circular Auto-Helix patterns, spiraling from the ground to 700 m AGL and then back down traversing the IOS-ES tower line, thus providing data from elevations that towers could not reach. A series of towers were also placed in a deep canyon close to IOS-ES for a special canyon flow experiment, which included smoke releases.

Some duplicate measurements were recorded at IOS within close proximity to each other, providing an opportunity for intercomparison of instruments and high-resolution spatiotemporal information.

Instruments were relocated as needed after preliminary data analysis, but exhaustive time demands on researchers did not leave much room for coeval data analysis.

IOPs and data. Each campaign included 10 IOPs where all instruments were operated in coordination. The core instruments (SAMS, mini-SAMS, PWIDS) and some selected observing platforms, however, were operated continuously. The IOPs were classified according to the synoptic wind speed (Table 1), and the IOP days were chosen a day earlier considering weather briefings by DPG forecasters with input from MATERHORN meteorologists as well as logistical and manpower constraints. The forecasting products employed included DPG's high-resolution Weather Research and Forecasting (WRF) Model–based advanced Four-Dimensional (4DWX) weather modeling system developed by NCAR (Liu et al. 2008), a 30-member 4DWX ensemble, North American Mesoscale (NAM), and Global Forecast System (GFS) model outputs as well as satellite products. A typical IOP lasted 24 h, although a few lasted longer or shorter. The data (~50 TB) are stored on a dedicated server at UND. The data will be released to the scientific community 3 years after the end of each experiment.

MATERHORN-M. The continuing work of MATERHORN-M seeks improvements in both mesoscale and submesoscale predictions. The model choices for the mesoscale are WRF and Coupled Ocean–Atmosphere Mesoscale Prediction System (COAMPS), but the focus hitherto has been on WRF, approaching from multiple angles using complementary efforts. To help instrumentation siting for campaigns, WRF was used to hindcast flow at DPG, which proved to be extremely useful. For example, the original design of IOS-ES assumed strong slope flows from ES-5 to ES-2 towers, and hence the combo (hot film/sonic) probe systems for turbulence (which require approach flow to be within approximately ±30° of the probe direction) were oriented accordingly. The simulations, however, indicated that downslope flows below ES-4 are quickly overshadowed by valley and secondary flows. This suggested reorientation of combos, thus circumventing a costly misperception. During campaigns, real-time WRF forecasts were made at high resolution (~1-km horizontal grid intervals), initialized four times per day (at 0000, 0600, 1800, and 2400 UTC). After the field programs, the forecasts were evaluated against observations, which has been particularly helpful in model performance evaluation and devising improvements (Pu et al. 2014).
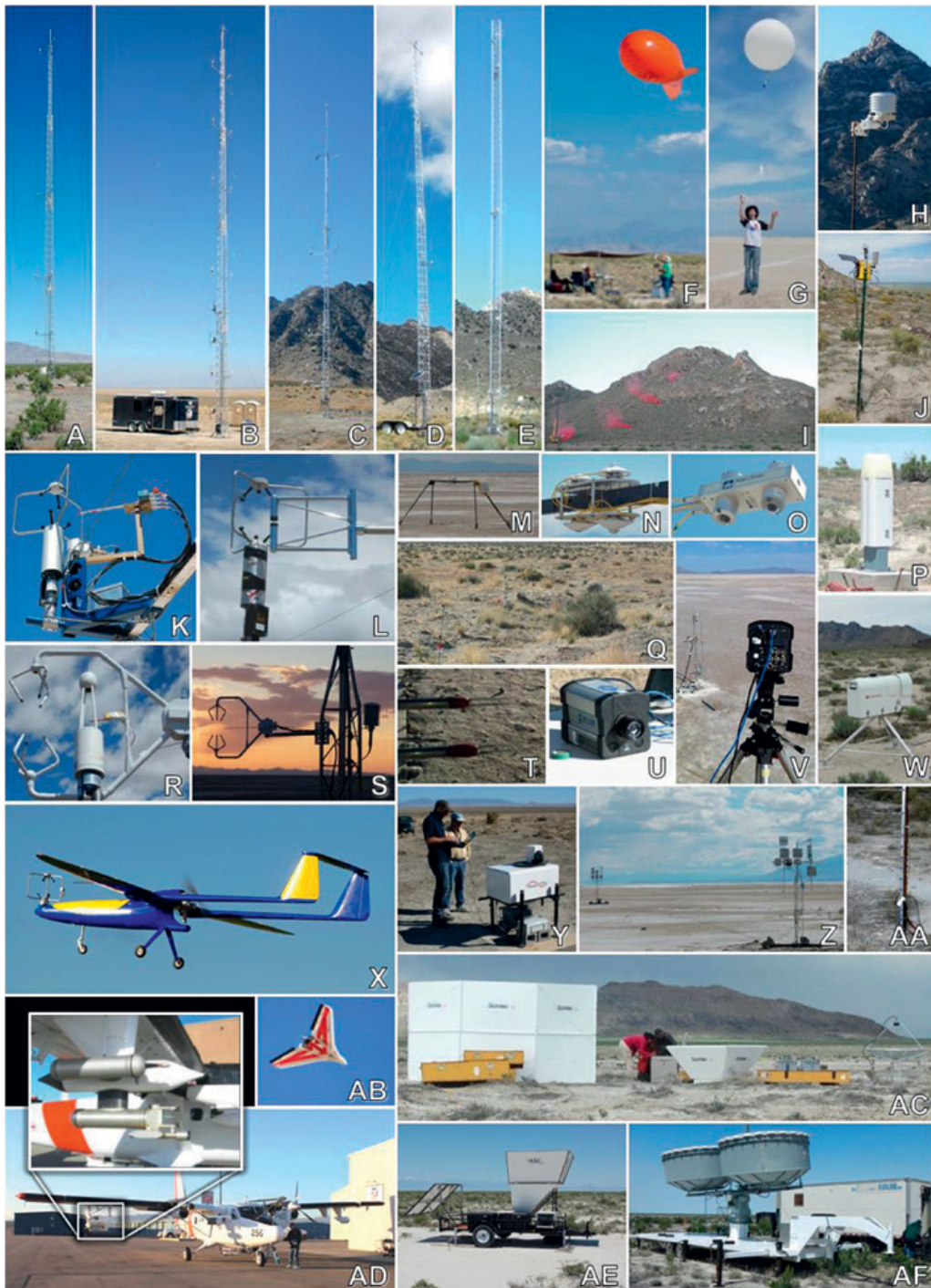
FIG. 4. Salient instruments at DPG: (a) ES-1; (b) ES-2; (c) ES-3; (d) ES-4; (e) ES-5; (f) tethered-balloon soundings; (g) radiosondes; (h) HOBO weather stations; (i) dividing streamline smoke release located on the northwest side of Granite Mountain; (j) LEMS weather stations; (k) 3D hot-film combo probe; (l) Krypton hygrometer; (m) radiation balance observations at IOS-Playa; (n) radiation balance observations at IOS-Sagebrush; (o) net radiometer as the tower-mounted component of the energy budget; (p) ceilometers; (q) distributed temperature sensing system (DTS); (r) infrared gas analyzers; (s) fine-wire thermocouples coupled with 3D sonic anemometers; (t) flux Richardson number hot-wire probe for near-ground measurements; (u) FLIR IR camera; (v) high-resolution near-surface thermal-image velocimetry; (w) microwave radiometer profiler; (x) Flamingo UAV; (y) scanning lidars; (z) RF polarimetric crosshairs surface moisture probes; (aa) array of fine-wire thermocouples, enhanced resolution near the ground; (ab) DataHawk UAV; (ac) SoDAR/RASS; (ad) Twin Otter with wind lidar (TODWL); (ae) mini-SoDARs; and (af) frequency-modulated continuous-wave radar (FM-CW) radar.

A number of studies were conducted to evaluate forecasting and data-assimilation skills of WRF. In one study, the relative performance of a 3D variational data-assimilation method and an ensemble Kalman filter (EnKF) assimilation over complex terrain was evaluated (Pu et al. 2013). In two other studies, the EnKF system developed by NCAR's Data Assimilation Research Testbed (DART; Anderson 2003; Anderson et al. 2009) was applied, assimilating radiosonde and surface observations from both campaigns. Errors in near-surface temperature and wind from WRF simulations in complex-terrain regions were also examined (Zhang et al. 2013; Zhang and Pu 2014). In two related studies, WRF biases due to poorly represented soil properties of DPG (Massey et al. 2014) as well as skills of PBL schemes (R. Dimitrova et al. 2015, manuscript submitted to *Bound.-Layer Meteor.*) were investigated.

Inspired by the rich observational datasets of MATERHORN, another study concerned ensemble sensitivity analysis (ESA) as an alternative to adjoint sensitivity, focusing on quiescent flow at DPG and over the Salt Lake Valley. It particularly dealt with model-based studies on sensor placement configurations to maximize forecast accuracy and to enable the capture of useful dynamical processes (Hacker and Lei 2015), the results of which could be applied to a future experiment that dealt with fog in complex terrain (MATERHORN-Fog). Methods for observing network design are immature at fine scales (e.g., 1–4-km horizontal grid spacing), during weak flows, and over complex terrain. ESA becomes inaccurate when the underlying assumptions of linear dynamics and Gaussian statistics are violated or when the sensitivity cannot be robustly sampled, and hence the limits of applicability of ESA were of interest.

For submesoscales, the emphasis is on the development of the IBM nested in WRF (i.e., for large-eddy simulations), enabling simulations over very steep slopes at very high resolutions (~10 m) using realistic atmospheric forcing. The goal is to achieve fully coupled mesoscale to microscale simulations without the undesirable numerical effects of terrain-following coordinates (Lundquist et al. 2010, 2012). Selecting the optimal transition point between the coordinate systems arguably minimizes model errors. The IBM method involves the use of a ghost-cell IBM that employs a Cartesian grid, where the effect of solid boundaries is realized by adding body forces, allowing the treatment of topography without terrain-following coordinates.

SOME PRELIMINARY FINDINGS. A few noteworthy outcomes of MATERHORN are

summarized below, and detailed results are expected to appear in special issues of AMS journals as well as *Boundary-Layer Meteorology* and *Environmental Fluid Mechanics*.

Forecasting challenges. The daily MATERHORN weather briefings often pointed to the difficulties of predicting mountain weather, especially in the DPG region where a rich variety of synoptic and mesoscale systems, fronts, and airmass boundaries influence the weather. Intermountain cyclones and cold fronts are most frequent and intense during the spring, and their evolution is strongly influenced by the upstream Sierra Nevada. Surface pressure troughs and associated low-level confluence (i.e., the Great Basin confluence zone; Steenburgh et al. 2009) that often extend northeastward from the Sierra Nevada to DPG can be accompanied by abrupt transitions in sensible weather and serve as a locus for cyclogenesis or frontogenesis (e.g., Jeglum et al. 2010; West and Steenburgh 2010, 2011). Interactions between synoptic and mesoscale weather systems and the DPG terrain led to hazardous weather at times, unforeseen owing to significant model forecast errors, posing major challenges for operations. For example, during the afternoon hours of spring IOP8, WRF called for a weak trough to move southward through GMAST with moderate (~5 m s^{-1}) northerly to northwesterly surface flow in its wake at 2200 UTC. Instead, this boundary was delayed, developed into a strong cold front, and moved through the GMAST domain with winds of approximately 15 m s^{-1} (Fig. 5), requiring an early termination of the IOP.

As a part of data-assimilation studies, a 1-month-long, 3-hourly continuous data assimilation and forecast cycle was conducted (Zhang and Pu 2014). The results illustrated that the quality of EnKF/WRF analysis is generally reasonable, and the short-range (3 h) forecast errors are comparable to those of NCEP's NAM forecasts for both 10-m wind speed and temperature. Since the latter sets the gold standard for operational forecasts, having EnKF/WRF performance statistically on par with NAM implies that substantial progress has been made with respect to EnKF/WRF; further improvements are continuing. With the data assimilation, the model reproduced reasonable forecasts of various synoptic and local flows, including mountain–valley circulations and frontal passages. The flow features over different land types were also distinguished.

Diurnally varying model biases for temperature and wind velocity were evident, especially in near-surface atmospheric predictions under quiescent

cases, consistent with other published work, indicating model inadequacies (Mass et al. 2002; Cheng and Steenburgh 2005; Hart et al. 2005; Zhang et al. 2013). Flow-dependent errors associated with flow transitions as well as strong synoptic forcing were also evident. Evaluations against synoptic-network and MATERHORN rawinsonde and tethersonde launches, nonetheless, showed that WRF is generally skilled in predicting conditions above the surface layer in complex terrain. Although wind predictions in the SBL were accurate, temperature predictions remained a challenge. Bias and RMSE during the night were approximately 2 and 4 K, respectively (Pu et al. 2014).

Ongoing modeling activities continue to highlight challenges faced by (Army) forecasters at DPG, whose tools include the GMAST observational network and the NCAR 4DWX. The latter employs data assimilation, cycling eight times a day at 1.1-km resolution, and it combines the WRF predictive core with current atmospheric conditions to make detailed predictions for the next several days. Because 4DWX uses WRF as its predictive core, MATERHORN WRF modelers' experiences were similar to DPG's experiences with 4DWX, such as an underpredicted diurnal cycle, biases in the near-surface wind speed, and insufficiently stratified conditions in the shallow SBL. The 30-member multiphysics ensemble version of 4DWX running at DPG mitigates the forecast errors that are rooted in specific physical parameterizations or sources of forcing at the boundaries. As the model–data comparison continues, our hypotheses for model shortcomings continue to unravel, pointing to problems of structure, physics, and parameterizations of WRF while defining avenues for improvements.

Scale symbiosis. The dense instrumentation permitted both individual- and multiple-scale processes studies. For example, Fig. 6 shows horizontal wind components taken by TODWL at two representative levels, selected from a series of measurements at about 2-km intervals in the horizontal with a vertical resolution of 50 m from about 250 m AGL to 500 m below the aircraft altitude. Note the coexisting flows at multiple scales, with upper-level synoptic flow (macro-β scale; Fig. 6a), near-surface northerly upvalley and upslope flows (meso-γ scale), flow channeling

TABLE 1. Classification of IOPs, dates, and types.		
IOP classification	**Definition (based on 700-hPa wind speed)**	
Quiescent	<5 m s^{-1}	
Moderate	5–10 m s^{-1}	
Transitional	Variable, >10 m s^{-1} possible with frontal passages	

Fall 2012 IOPs		
IOP	**Period**	**Type**
0	1400 MDT 25 Sep–1400 MDT 26 Sep	Quiescent
1	1400 MDT 28 Sep–1400 MDT 29 Sep	Quiescent
2	1400 MDT 1 Oct–1400 MDT 2 Oct	Quiescent
3	0200 MDT 3 Oct–0200 MDT 4 Oct	Transitional
4	1400 MDT 6 Oct–1400 MDT 7 Oct	Moderate
5	1400 MDT 9 Oct–1400 MDT 10 Oct	Transitional (quiescent–moderate)
6	0200 MDT 14 Oct–0200 MDT 15 Oct	Quiescent
7	1200 MDT 17 Oct–2000 MDT 17 Oct	Transitional (quiescent–moderate)
8	0500 MDT 18 Oct –1200 MDT 19 Oct	Quiescent
9	1400 MDT 20 Oct –1400 MDT 21 Oct	Moderate

Spring 2013 IOPs		
IOP	**Period**	**Type**
1	1400 MDT 1 May–1400 MDT 2 May	Transitional (moderate–quiescent)
2	1400 MDT 4 May–1400 MDT 5 May	Moderate
3	0500–1700 MDT 7 May	Moderate
4	1400 MDT 11 May–1400 MDT 12 May	Quiescent
5	1200 MDT 13 May–1200 MDT 14 May	Transitional (moderate–quiescent)
6	1200 MDT 16 May–1200 MDT 17 May	Transitional (moderate–quiescent)
7	1715 MDT 20 May–1400 MDT 21 May	Quiescent
8	1400 MDT 22 May–1400 MDT 23 May	Moderate
9	1000 MDT 25 May–1000 MDT 26 May	Moderate
10	1400 MDT 30 May–1000 MDT 31 May	Moderate

through the small gap (micro-α scale), and vortex structures (micro-β scale) formed in the mountain wake (Fig. 6b). Yet, flow patterns in the two basins maintained their own unique characteristics; for example, as evidenced later, they have different PBL heights and microcirculation features. WRF 4DWX could predict the overall flow patterns, including the flow distortion by GM, but as expected finer features such as vortex structures and in-canyon flows could not be captured (Fig. 6c).

Surface energy budget and soil property differences. Measurements of individual components of radiation, surface energy budget (SEB), and related variables at three representative locations (IOS-Sagebrush, IOS-Playa, and ES-5) revealed the role of soil thermal property (e.g., thermal conductivity) gradients, which dictate the ground heat flux and hence the soil moisture content (Table ES1). Soil moisture content and its spatial variability were much higher at the IOS-Playa than at the other two sites, thus creating a larger energy sink during the day. This is due to the shallow water table at IOS-Playa (~80 cm from the surface) during the spring compared to the other two sites with much deeper water tables (deeper than 200 cm; Soil Survey Staff 2014). The heat stored in the Playa was released during the night, leading to higher surface temperatures and longwave radiation emissions.

The importance of soil properties was also accentuated by MATERHORN-M (Massey et al. 2014). It is known that the near-surface (2 m) temperature forecasts of WRF over the western United States, as well as by other modeling systems applied to various regions of the world, frequently underpredict the diurnal cycle with a strong nocturnal warm bias (Mass et al. 2002; Hart et al. 2005; Kilpelainen et al. 2012; Ngan et al. 2013; Zhang et al. 2013). Existing hypotheses concerning these forecast errors range from inadequate horizontal or vertical resolution to the inaccurate initialization and parameterization of the boundary layer to the land surface characteristics and processes (e.g., Hanna and Yang 2001; Marshall et al. 2003; Cheng and Steenburgh 2005). Using surface observations, soil observations from the U.S. Department of Agriculture's Soil Climate Analysis Network (SCAN). and SEB collected during the fall campaign, a pronounced nocturnal warm bias was identified over areas with silt loam and sandy loam soils at DPG (Massey et al. 2014). This bias could be traced to errors in the initialization of soil moisture and parameterization of soil thermal conductivity. WRF forecasts of nocturnal surface temperature as well as the predicted ground heat flux, soil thermal conductivity, and near-surface radiative fluxes could be improved by initializing with measured soil moisture and replacing the Johansen (1975) parameterization for soil thermal conductivity in the Noah land surface model with that proposed by McCumber and Pielke (1981) for silt loam and sandy loam soils. We anticipate similar improvements for other arid regions during periods of low soil moisture.

Surface-layer similarity theory. The Monin–Obukhov similarity theory (MOST) has been extensively discussed and evaluated (e.g., Foken 2006), but questions linger on its applicability to complex terrain and morning and/or evening transition periods, as both violate the basic tenets of MOST—that is, stationarity and horizontal homogeneity of the flow. Yet, models continue to use MOST in a local sense, conveniently overlooking its limitations. During the BLLAST campaign in France, Blay-Carreras et al. (2014) observed near-surface countergradient behavior of sensible heat fluxes during the evening transition, when the MOST stability functions also deviated greatly from (neutrally stable) idealized
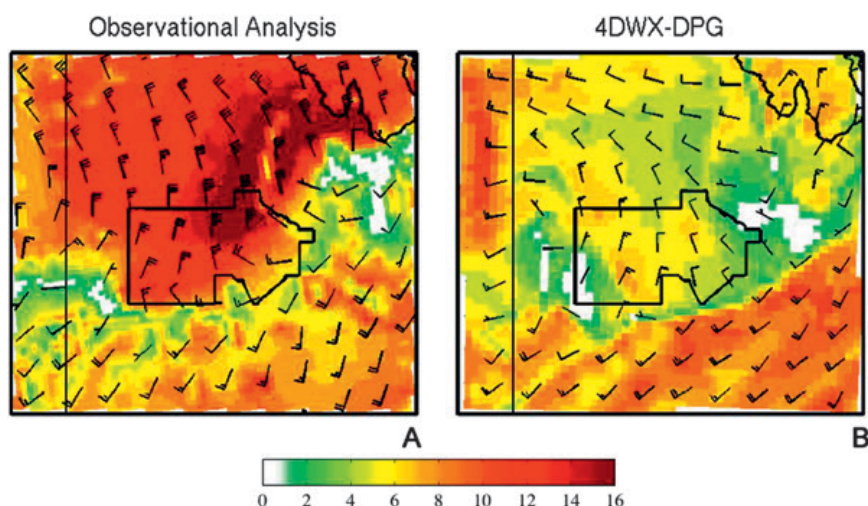

Fig. 5. (a) Analyzed and (b) 14-h WRF 4DWX forecast of 10-m wind speeds at DPG depicted using a color scale (shown below, m s^{-1}) and wind barbs (full and half barb denote 5 and 2.5 m s^{-1}, respectively) at 2200 UTC 22 May 2013, during IOP8.
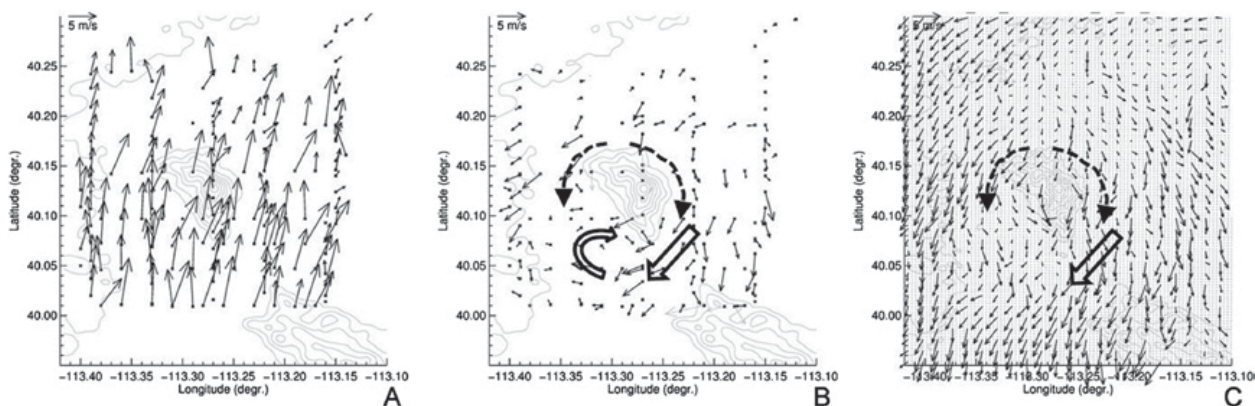
FIG. 6. Example of TODWL data obtained, 9 Oct 2012, during IOP 5, in the afternoon at 3000 m MSL representing (a) upper-level flow at 1750 m MSL, (b) near-surface flow, and (c) 300-m-resolution simulations of near-surface flow for the same time (1700 MDT) using WRF. The arrows indicate recurring surface flow patterns in the afternoon boundary layer around Granite Mountain.

profiles typically used in weather prediction models (Smedman et al. 2007). A similar behavior was also observed during MATERHORN-X at all of the flux sites. An intriguing result, in addition, was the nature of transition over surfaces with very different thermal characteristics (Jensen et al. 2015, manuscript submitted to *Bound.-Layer Meteor.*). Below 5 m, at the vegetated IOS-Sagebrush, the local temperature gradient changed sign after the flux changed sign, while at the Playa site the gradient preceded the flux reversal. At each of the sites, the fluxes at all heights in the lower 20 m appear to change the sign roughly at the same time. Both countergradient situations lead to similar deviations from MOST, but at different times owing to the large thermal storage of the Playa. The abrupt collapse of turbulence observed during evening transition points to the inapplicability of MOST for transition periods (even in a local sense), calling for further studies on the (evening) collapse of convective turbulence under different land-use conditions. The dependence of turbulence collapse on overlying capping inversions (Caughey and Kaimal 1977) and surface characteristics (Cole and Fernando 1998) has been pointed out in previous work, and our database offers opportunities for delving into such intricacies.

Evening transition. The evening transition is rich in interesting physics, depending on the slope, vigor of prior convection, land use, shading, and existing local flows. At the outset, it was hypothesized that the temperature jump across a shadow front (leading edge of a moving shadow created by the obstruction of sunlight by topography), similar to that observed by Nadeau et al. (2013) in the Swiss Alps and Katurji et al. (2013) in Antarctica, would dominate the transitional behavior. Such a behavior was indeed

found during a quiescent IOP of the spring field campaign, where transition followed the shadow front down the slope (Lehner et al. 2015). For the fall campaign, however, the data indicated otherwise; that is, two flow transition types (front and cooling slab) discussed and illustrated recently by Fernando et al. (2013) were present at IOS-ES, uncorrelated with the passage of the shadow front. When present, the transition front originated upslope of the observation towers and moved downslope, sequentially switching the wind direction of towers and intensifying turbulence, and these observations have some consistency with the mechanism proposed by Hunt et al. (2003). The DTS measurements of near-surface temperature vividly confirmed the frontal propagation (Fig. 7), where the lower (0.5 m) air layer showed progressive cooling due to the front arrival in consonance with the flow-reversal data of towers. The front had an inclined nose, as evident from the reversal times at different heights (not shown). During slab transitions, winds of all towers reversed simultaneously as if a slab of dense fluid slid down the slope. Both mechanisms were found to exist in approximately equal numbers during quiescent IOPs in the fall.

The investigations of morning transition were focused on physical mechanisms and processes—for example, those proposed by Whiteman (1982) and Princevac and Fernando (2008). The former is based on the growth of CBL within the valley and simultaneous generation of an upslope flow that causes the stable core aloft the CBL to descend; the collusion between the two promotes the breakup of nocturnal stratification. Princevac and Fernando (2008) proposed that intrusions shaving off the upslope flow (see Fig. 1) may entrain into the growing CBL, thus providing an
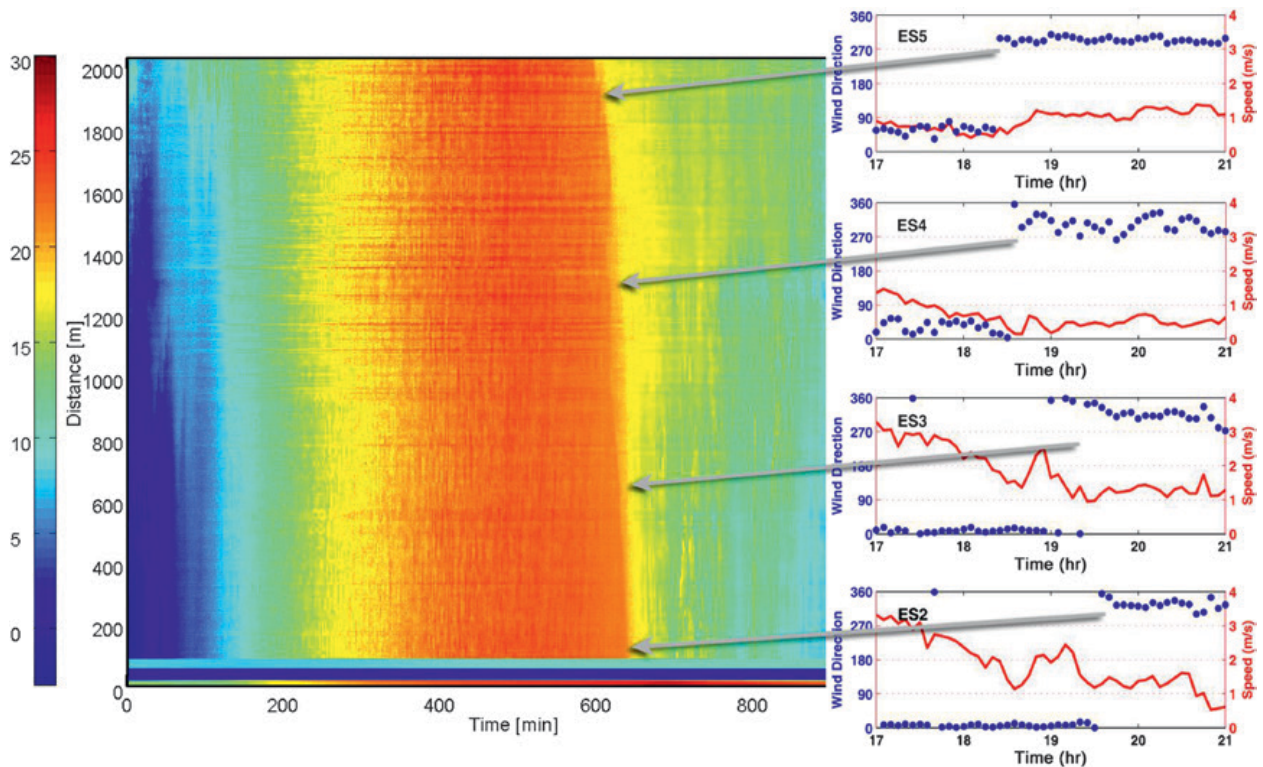
FIG. 7. Near-surface (0.5 m AGL) temperature measurements by DTS installed on the east slope of Granite Mountain on 9 Oct 2012 (IOP 5). DTS spanned a 2-km transect between towers ES-2 and ES-5. The timeline starts at local sunrise, determined using radiation measurements at ES-5 (located about 2000 m on the ordinate in this plot). The wind direction and speed are shown to the right for ES-2–ES-5, and the change of wind direction roughly coincided with the drop of local temperature. There is a progression of temperature drops from ES-5 to ES-2.

additional breakup mechanism. Figure 7 shows that the morning warming at the east slope site first occurs close to the foothills, impeding the flow draining from high to low slopes, and continues down the slope with time. Wind transitions in the presence of slope breaks and spatially inhomogeneous surface warming have not been investigated, and our data repository offers a range of kindred research opportunities.

Flows in the basins. The basinwide stratification is dependent on the spatial distribution of SEB, basin morphology, and large-scale forcing. Tethered-balloon flights in the east and west basins during quiescent IOPs demonstrated the differences of stratification and SBL height. Southeasterly flows originating at the Dugway Valley and the slopes of the Simpson, Keg, and Thomas Mountains travel to the east of GM, while southerly flows on the west of GM originate at the Fish Springs Flat and upstream Snake Valley. The two sides communicate through intermountain (big and small) gaps. Figure 8 shows the measured vertical structure of fully established nocturnal downvalley flow in the basins, where a low-level jet is evident.

The IOS-Sagebrush exhibits much cooler surface temperatures and a strong low-level elevated capping inversion that prevents the surface jet from mixing vertically. The larger ground heat flux at IOS-Playa leads to warmer nighttime surface temperatures than at Sagebrush, allowing the nocturnal jet to mix deeper aloft.

The two sites were simulated using WRF, where the modified land surface model of Massey et al. (2014) described earlier was employed but with a different model initialization (GFS) and without soil moisture assimilation. Six default PBL schemes were used, and starkly different predictions were obtained. The predictions based on Yonsei University (YSU) and quasi-normal-scale elimination (QNSE) (default) schemes are shown in Fig. 8, selected considering their performance statistics at 10 m. QNSE was found to perform better for the near-surface temperature (at 2 m) compared to YSU that performed better for the wind speed (at 10 m). Overall, the relative performance of PBL schemes depended on the type of observation and the height range used for statistics [see the caption and R. Dimitrova et al. (2015, manuscript
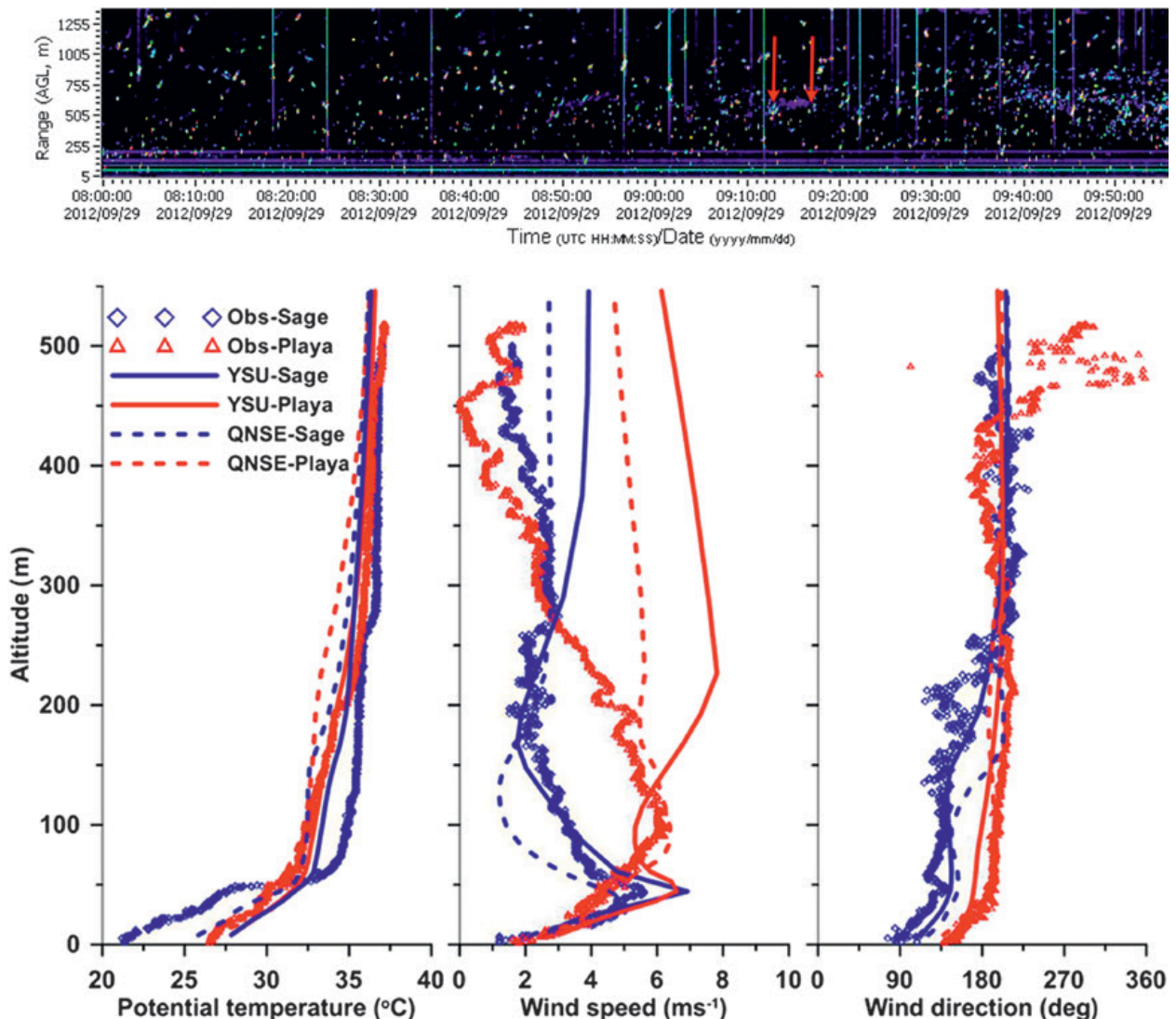
Fɪɢ. 8. (bottom) Comparison of the wind and temperature structure of the nocturnal SBL at IOS-Playa and IOS-Sagebrush during IOP1 on 29 Sep 2012. The profiles are compared with WRF (500-m grid size) simulations with two PBL schemes: YSU and QNSE schemes. Tethered-balloon ascent time is 0907–0927 UTC (0307–0327 MDT). Model output is averaged over 0000–0920 UTC (0300–0320 MDT). Six default PBL schemes in WRF were attempted, and two were selected based on overall statistical performance using data at 10 m. For the example shown, YSU provides the best overall performance up to 200 m and QNSE performs better beyond 200 m. (top) Power backscatter signal from FM-CW radar indicates a developing inversion at approximately 500 m during the measurement period (arrows), which was not captured by the simulations.

submitted to *Bound.-Layer Meteor.*)]. In addition, the performance is expected to be sensitive to the basin configuration, since nuances of flow physics therein determine the efficacy of a particular PBL scheme.

A warm bias appeared near the surface, although the predictions of wind speed and direction were satisfactory. The YSU scheme predicted the position but not the magnitude of the Sagebrush jet, while overall disparities for IOS-Playa jet were marked. The wind direction was reasonably well predicted by both schemes over the entire 500-m column measured by

tethered balloons. FM-CW radar showed a developing inversion above the approximately 500-m level, just above the ceiling of balloon flights, but this feature was not captured by WRF. Such disparities call for continued improvements of PBL schemes for SBL.

On the other hand, the observed differences of key variables between the east and west basins were reduced during the convective period, facilitated by significant exchange of air between them (i.e., exchange flows) through the big and small gaps (Fig. 6). Nevertheless, some differences were still noticeable.

This is evident from Fig. 9, where concurrent CBL measurements using TODWL and Datahawk UAV are shown for morning flights of fall IOP5, with terrain-following PBL heights derived from the aerosol backscatter profiles. A consistent picture emerges with PBL heights 100–300 m AGL, indicating evolving convective boundary layer with appreciable differences in CBL heights between the basins.

Slope and valley flow interactions. Valley circulations that develop on either side of Granite Mountain during quiescent IOPs are likely to be modulated by differential thermal forcing, for example, owing to the land surface contrast between sparsely vegetated areas to the southeast and the playa to the northwest (Rife et al. 2002). Adding to the complexity is the vacillating interbasin air exchange through the small and big gaps; see Figs. 3 and ES1. Air exchange through the narrow gap increases turbulence and vertical mixing when the flow is fanning out from the gap and when horizontal shear layers develop within the gap periodically.

An interesting valleywide flow interaction phenomenon was observed during quiescent IOPs, when a southeasterly downvalley flow in the Dugway basin merged with southwesterly flow through the big gap. The vorticity that develops during this confluence acted to steer the colder air of the valley flow toward the (relatively warmer) katabatic flow on the eastern slope of GM, leading to collision of two counterflows. A set of small-scale processes (turbulence, instabilities, and intrusions) emerged during collisions, enhancing the local subgrid-scale heat and momentum transfer. The corresponding lidar scans and laser-illuminated smoke visualization along the ES tower line are shown in Figs. 10a,c. Figure ES2 presents a movie of smoke flow visualization. Figure 10b depicts a controlled laboratory experiment designed to mimic the collisions and parameterize observed high turbulent intensities and fluxes (Fig. 10d).

The impact of collisions leads to rapid hydraulic adjustment in the basin flow, prompting the flushing of the basin on the north side while generating basin-scale oscillations (seiching), as evinced by IR imaging. As the colder air that had been pushed up the slope recedes back out into the basin, it is met by a reestablishing valley flow after the collision. This collision cycle repeated numerous times during quiescent evenings (Fig. 10d).
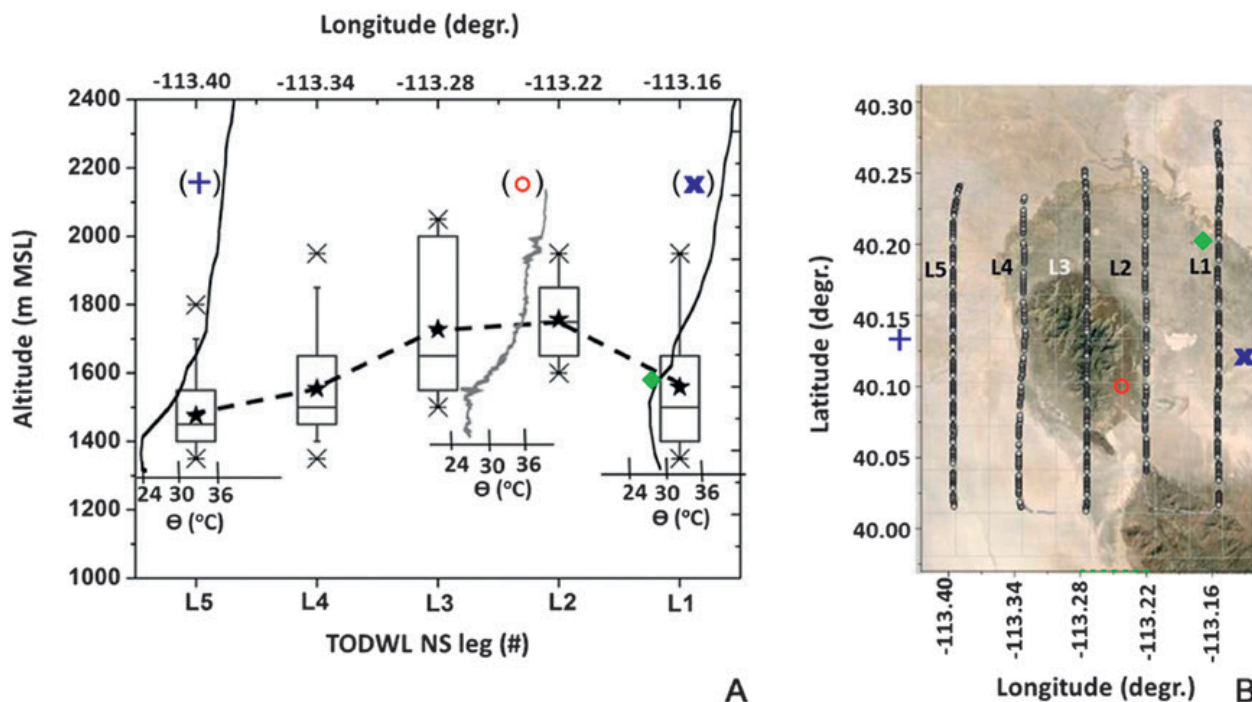

FIG. 9. (a) Box-and-whisker plot of CBL heights derived from aerosol backscatter profiles along the (b) north–south TODWL flight legs. The data were collected during a morning mission between 1012 and 1052 MDT 10 Oct 2012. The horizontal line in the box and the bottom and top lines of the box show the median of the data and the lower and upper quartiles (25% and 75%), respectively. The whiskers show the minimum and maximum values while * is the mean value. Potential temperature profiles from the radiosondes at the Playa (+) and Sagebrush (×) sites, a DATAHAWK UAV (O) profile near the ES-2 tower, and the CBL height based on FM-CW radar (♦) are shown in (a).

Similar flow collisions appeared in other locations that are conducive for opposing flows, as indicated by the decomposition of valley flow into topological structures (Fig. 10e) using the proper orthogonal decomposition (POD) technique (Adrian et al. 2000). In general, collisions appear to be distributed over space and time within the SBL. WRF and other mesoscale models do not account for such spasmodic subgrid heat and/or momentum flux–generating processes, and their incorporation through conditional parameterizations is
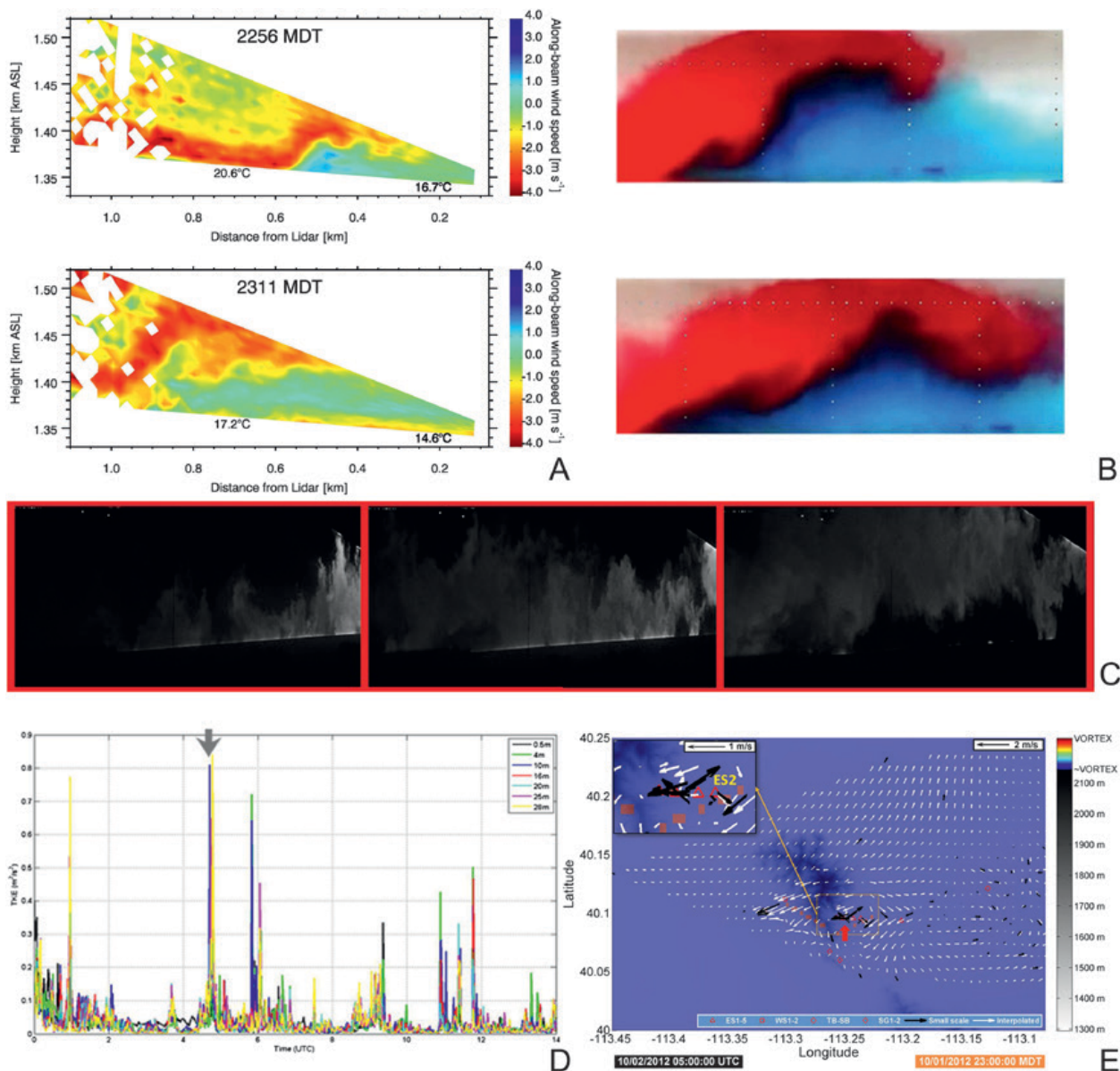
FIG. 10. A collision event during fall IOP2. (a) Lidar scans (located near ES-2) captured the collision between the downslope flow (red) and valley flow (blue), with the latter arriving almost normal to the slope because of its modification by the gap flow. Upon collision, the denser fluid undercuts the lighter fluid. (b) A laboratory experiment on collision of lighter (red) and denser (blue) fluids. Intense small-scale mixing is evident in (a) and (b). (c) A collision captured by smoke visualization on the slope (initially smoke travels to the right, downslope, and denser smoke-free flow undercuts it); the lower limit of beam does not coincide with the ground (see movie in Fig. ES2). (d) Collisions are temporally intermittent and associated with a rapid rise of turbulent kinetic energy (TKE), as evidenced by ES-2 anemometers. Arrow corresponds to the event in (a). (e) Collision events educed using the POD technique. The measured vector field (black) by towers and PWIDS is decomposed to small- and large-scale fields using POD, and the interpolated small-scale field is shown (white). The red arrow shows the collision area in (a), which is rich in smaller scales. Collisions were spatially distributed over the Dugway Valley, as evident from flow convergence and/or stagnation areas.

crucial for modeling of mountain terrain winds. To this end, a comprehensive laboratory experiment is being conducted to develop parameterizations for fluxes associated with the collisions as a function of governing dimensionless variables and delineate conditions for productive (high flux) collisions.

Instrumentation siting for forecast accuracy. The ESA performed to guide the MATERHORN-Fog campaign (successfully conducted in January 2015) provides an example of ESA's utility. It concerned a fog event over the Salt Lake City airport (SLC), an area with frequent wintertime fog affected by complex terrain and the site for MATERHORN-Fog. Perfect-model ensemble data-assimilation experiments using DART and realistic upper-air observing network provided the statistics for ESA. Results showed that water vapor mixing ratios over SLC are sensitive to temperature on the first model layer tens of kilometers away, 6 h prior to verification, and before the onset of fog (Wile et al. 2015). Sensitivity 12 h prior was weaker but led to qualitatively similar results. Temperatures were a predictor of inversion strength in the Salt Lake basin; the ESA linked fog to southerly flow that strengthened inversions. In linearity tests, small perturbations did not lead to the expected forecast change, but larger perturbations did, suggesting that noise can dominate a small perturbation in weak flow conditions. Variations in the ESA as a function of ensemble size confirmed that the sensitivities are more difficult with smaller ensembles when flows are weak (Fig. 11). All of the linear ESA estimates systematically overpredicted the actual response to a perturbation, consistent with sampling error in estimates derived from a finite ensemble. Results from the ESA for fog over SLC motivated theoretical work as well as

experiments with a simple model to elucidate the role of both sampling error and a commonly used approximation in ESA (Hacker and Lei 2015). Ensuing results showed that sampling error can be mitigated by reducing regression coefficients according to the expected error in the sensitivities and that the approximation can be easily avoided through a minimum-norm regression. Including full spatial analysis covariance information, and accounting for sampling error, improved the ESA predictions for where observations are most likely to reduce forecast uncertainty.

SUMMARY. MATERHORN is truly a multidisciplinary effort, where a group of physical scientists and engineers collaborate across disciplines to create knowledge and develop tools to help improve weather prediction in mountain terrain (see www.nd.edu/~dynamics/materhorn). It has four components: modeling (M), experimental (X), technology (T), and parameterization (P). From the inception, MATERHORN-M was active, collaborated with stakeholders, and provided useful insights for experimental planning and development of hypotheses. Noticeable forecast improvements for WRF were realized using new land surface parameterizations with improved soil moisture and thermodynamic representations. Ensemble sensitivity runs were conducted and a localization theory was derived. The degree of usefulness of data assimilation was evaluated, and new assimilation techniques are being attempted. The modeling realm is being extended to ultra-high-resolution simulations via immersed boundary methods implemented in WRF.

MATERHORN-X delved into eight orders of spatial scales (10^{-3}–10^5 m, from Kolmogorov to mesoscales) and five orders of temporal scales (1–10^5 s). The most extensive are the first two field campaigns conducted in a secure, richly instrumented, complex-terrain test bed (Fernando and Pardyjak 2013), novel results of which were emphasized in this report. MATERHORN-T developed new sensor systems for moisture, fog, and turbulence as well as novel retrieval
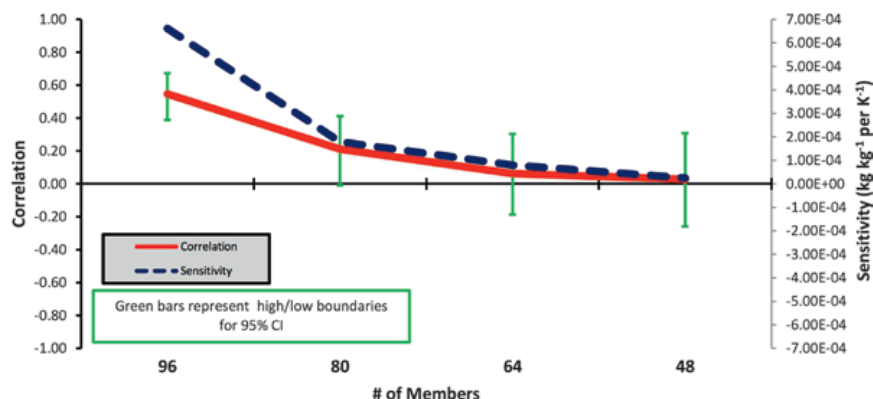
FIG. 11. The 6-h correlation (red) and ensemble sensitivity (blue) vs the number of ensemble members for a single point of positive sensitivities at 39.5°N, 112.9°W. Green bars indicate the 95% confidence interval. Correlations and covariances, underpinning the ensemble sensitivities, are more difficult to detect with smaller ensembles.

algorithms. The data are being extensively used for gaining physical insights, process studies, and model improvements. MATERHORN-P continues to verify existing parameterizations and develop new ones that are being implemented in WRF. The project has entered its data processing and intensive modeling phases at full steam. The overall theoretical, numerical, and technological development efforts as well as the massive dataset collected are expected to help future research in mountain meteorology immensely.

REFERENCES

Adrian, R. J., K. T. Christensen, and Z.-C. Liu, 2000: Analysis and interpretation of instantaneous turbulent velocity fields. *Exp. Fluids,* **29,** 275–290, doi:10.1007/s003489900087.

Albini, F. A., D. J. Latham, and R. G. Baughman, 1982: Estimating upslope convective wind speeds for predicting wildland fire behavior. USDA Forest Service Intermountain Forest and Range Experiment Station Research Paper INT-257, 19 pp.

Allwine, K. J., J. H. Shinn, G. E. Streit, K. L. Clawson, and M. Brown, 2002: Overview of URBAN 2000: A multiscale field study of dispersion through an urban environment. *Bull. Amer. Meteor. Soc.,* **83,** 521–536, doi:10.1175/1520-0477(2002)083<0521:OOUAMF>2.3.CO;2.

Anderson, J. L., 2003: A local least squares framework for ensemble filtering. *Mon. Wea. Rev.,* **131,** 634–642, doi:10.1175/1520-0493(2003)131<0634:ALLSFF>2.0.CO;2.

——, T. Hoar, K. Raeder, H. Liu, N. Collins, R. Torn, and A. Avellano, 2009: The Data Assimilation Research Testbed: A community facility. *Bull. Amer. Meteor. Soc.,* **90,** 1283–1296, doi:10.1175/2009BAMS2618.1.

Baines, P. G., 1979: Observations of stratified flow past three-dimensional barriers. *J. Geophys. Res.,* **84,** 7834–7838, doi:10.1029/JC084iC12p07834.

——, 1998: *Topographic Effects in Stratified Flows.* Cambridge University Press, 482 pp.

Banta, R. M., 1984: Daytime boundary-layer evolution over mountainous terrain. Part I: Observations of the dry circulations. *Mon. Wea. Rev.,* **112,** 340–356, doi:10.1175/1520-0493(1984)112<0340:DBLEOM>2.0.CO;2.

——, Y. L. Pichugina, N. D. Kelley, R. M. Hardesty, and W. A. Brewer, 2013: Wind energy meteorology: Insight into wind properties in the turbine-rotor layer of the atmosphere from high-resolution Doppler lidar. *Bull. Amer. Meteor. Soc.,* **94,** 883–902, doi:10.1175/BAMS-D-11-00057.1.

Barry, R. G., 2008: *Mountain Weather and Climate.* 3rd ed. Cambridge University Press, 512 pp.

Belcher, S. E., and J. C. R. Hunt, 1998: Turbulent flow over hills and waves. *Annu. Rev. Fluid Mech.,* **30,** 507–538, doi:10.1146/annurev.fluid.30.1.507.

Bjerknes, and Coauthors, 1934: For mountain observatories. *Bull. Amer. Meteor. Soc.,* **15,** 993–994.

Blay-Carreras, E., E. R. Pardyjak, D. Pino, D. C. Alexander, F. Lohou, and M. Lothon, 2014: Countergradient heat flux observations during the evening transition period. *Atmos. Chem. Phys.,* **14,** 9077–9085, doi:10.5194/acp-14-9077-2014.

Blumen, W., Ed., 1990: *Atmospheric Processes over Complex Terrain. Meteor. Monogr.,* No. 45, Amer. Meteor. Soc., 323 pp.

Boettinger, J. L., 2009: Soils of Utah. Rangeland resources of Utah, Utah State University Extension Cooperative Extension Doc., 46–48. [Available online at https://extension.usu.edu/utahrangelands/files/uploads/RRU_Final.pdf.]

Brighton, P. W. M., 1978: Strongly stratified flow past three-dimensional obstacles. *Quart. J. Roy. Meteor. Soc.,* **104,** 289–307, doi:10.1002/qj.49710444005.

Caughey, S. J., and J. C. Kaimal, 1977: Vertical heat flux in the convective boundary layer. *Quart. J. Roy. Meteor. Soc.,* **103,** 811–815, doi:10.1002/qj.49710343821.

Cheng, W. Y. Y., and W. J. Steenburgh, 2005: Evaluation of surface sensible weather forecasts by the WRF and

the Eta models over the western United States. *Wea. Forecasting,* **20,** 812–821, doi:10.1175/WAF885.1.

Chow, F. K., S. F. J. De Wekker, and B. Snyder, Eds., 2013: *Mountain Weather Research and Forecasting: Recent Progress and Current Challenges.* Springer, 750 pp., doi:10.1007/978-94-007-4098-3.

Clements, C. B., C. D. Whiteman, and J. D. Horel, 2003: Cold-air-pool structure and evolution in a mountain basin: Peter Sinks, Utah. *J. Appl. Meteor.,* **42,** 752–768, doi:10.1175/1520-0450(2003)042<0752:CSAEIA>2.0.CO;2.

Cole, J. S., and H. J. S. Fernando, 1998: Some aspects of the decay of convective turbulence. *Fluid Dyn. Res.,* **23,** 161–176, doi:10.1016/S0169-5983(97)00051-8.

Deardorff, J. W., 1970: Convective velocity and temperature scales for the unstable planetary boundary layer and for Rayleigh convection. *J. Atmos. Sci.,* **27,** 1211–1213, doi:10.1175/1520-0469(1970)027<1211:CVATSF>2.0.CO;2.

De Wekker, S. F. J., K. Godwin, G. D. Emmitt, and S. Greco, 2012: Airborne Doppler lidar of valley flows in complex coastal terrain. *J. Appl. Meteor. Climatol.,* **51,** 1558–1574, doi:10.1175/JAMC-D-10-05034.1.

Doran, J. C., J. D. Fast, and J. Horel, 2002: The VTMX 2000 campaign. *Bull. Amer. Meteor. Soc.,* **83,** 537–551, doi:10.1175/1520-0477(2002)083<0537:TVC>2.3.CO;2.

Eaton, F. D., S. A. McLaughlin, and J. R. Hines, 1995: A new frequency-modulated continuous wave radar for studying planetary boundary layer morphology. *Radio Sci.,* **30,** 75–78, doi:10.1029/94RS01937.

Ellis, A. W., M. L. Hilderbrandt, W. Thomas, and H. J. S. Fernando, 2000: A case study of the climatic mechanisms contributing to the transport of lower atmospheric ozone across metropolitan Phoenix area. *J. Climate Res.,* **15,** 13–31, doi:10.3354/cr015013.

Fernando, H. J. S., 2010: Fluid dynamics of urban atmospheres in complex terrain. *Annu. Rev. Fluid Mech.*, **42,** 365–389, doi:10.1146/annurev-fluid-121108-145459.

——, and J. C. Weil, 2010: Whither the stable boundary layer? A shift in the research agenda. *Bull. Amer. Meteor. Soc.,* **91,** 1475–1484, doi:10.1175/2010BAMS2770.1.

——, and E. R. Pardyjak, 2013: Field studies delve into the intricacies of mountain weather. *Eos, Trans. Amer. Geophys. Union,* **94,** 313–315, doi:10.1002/2013EO360001.

——, B. Verhoef, S. Di Sabatino, L. S. Leo, and S. Park, 2013: The Phoenix Evening Transition Flow Experiment (TRANSFLEX). *Bound.-Layer Meteor.,* **147,** 443–468, doi:10.1007/s10546-012-9795-5.

Foken, T., 2006: 50 years of the Monin–Obukhov similarity theory. *Bound.-Layer Meteor.,* **119,** 431–447, doi:10.1007/s10546-006-9048-6.

Grubišić, V., and Coauthors, 2008: The Terrain-Induced Rotor Experiment: An overview of the field campaign and some highlights of special observations. *Bull. Amer. Meteor. Soc.,* **89,** 1513–1533, doi:10.1175/2008BAMS2487.1.

Hacker, J. P., and L. Lei, 2015: Multivariate ensemble sensitivity with localization. *Mon. Wea. Rev.,* **143,** 2013–2027, doi:10.1175/MWR-D-14-00309.1.

Hanna, S. R., and R. Yang, 2001: Evaluations of mesoscale models' simulations of near-surface winds, temperature gradients, and mixing depths. *J. Appl. Meteor.,* **40,** 1095–1104, doi:10.1175/1520-0450(2001)040<1095:EOMMSO>2.0.CO;2.

Hart, K. A., W. J. Steenburgh, and D. J. Onton, 2005: Model forecast improvements with decreased horizontal grid spacing over finescale intermountain orography during the 2002 Olympic Winter Games. *Wea. Forecasting,* **20,** 558–576, doi:10.1175/WAF865.1.

Hocut, C. M., 2013: Multi-scale flow and turbulence in complex terrain under weak synoptic conditions. Ph.D. dissertation, University of Notre Dame, 163 pp.

——, D. Liberzon, and H. J. S. Fernando, 2015: Separation of upslope flow over a uniform slope. *J. Fluid Mech.,* **775,** 266–287, doi:10.1017/jfm.2015.298.

Hunt, J. C. R., H. J. S. Fernando, and M. Princevac, 2003: Unsteady thermally driven flows on gentle slopes. *J. Atmos. Sci.,* **60,** 2169–2182, doi:10.1175/1520-0469(2003)060<2169:UTDFOG>2.0.CO;2.

——, A. Orr, J. W. Rottman, and R. Capon, 2004: Coriolis effects in mesoscale flows with sharp changes in surface conditions. *Quart. J. Roy. Meteor. Soc.,* **130,** 2703–2731, doi:10.1256/qj.04.14.

——, G. G. Vilenski, and E. R. Johnson, 2006: Stratified separated flow around a mountain with an inversion layer below the mountain top. *J. Fluid Mech.,* **556,** 105–119, doi:10.1017/S0022112006009335.

Jannuzzi, J. A., 1993: The onshore push of marine air into the Pacific Northwest. *Wea. Forecasting,* **8,** 194–203, doi:10.1175/1520-0434(1993)008<0194:TOPOMA>2.0.CO;2.

Jeglum, M. E., W. J. Steenburgh, T. P. Lee, and L. F. Bosart, 2010: Multi-reanalysis climatology of intermountain cyclones. *Mon. Wea. Rev.,* **138,** 4035–4053, doi:10.1175/2010MWR3432.1.

Johansen, O., 1975: Thermal conductivity of soils. Ph.D. thesis, University of Trondheim, 671 pp. [Available from Universitetsbiblioteket i Trondheim, Høgskoleringen 1, 7034 Trondheim, Norway.]

Katurji, M., P. Zawar-Reza, and S. Zhong, 2013: Surface layer response to topographic solar shading in Antarctica's dry valleys. *J. Geophys. Res. Atmos.,* **118,** 12 332–12 344, doi:10.1002/2013JD020530.

Kilpelainen, T., and Coauthors, 2012: Modelling the vertical structure of the atmospheric boundary layer over Arctic fjords in Svalbard. *Quart. J. Roy. Meteor. Soc.,* **138,** 1867–1883, doi:10.1002/qj.1914.

Kit, E., A. Cherkassy, T. Sant, and H. J. S. Fernando, 2010: In situ calibration of hot-film probes using a colocated sonic anemometer: Implementation of a neural network. *J. Atmos. Oceanic Technol.,* **27,** 23–41, doi:10.1175/2009JTECHA1320.1.

Lehner, M., C. D. Whiteman, S. W. Hoch, D. Jensen, E. R. Pardyjak, L. S. Leo, S. Di Sabatino, and H. J. S. Fernando, 2015: A case study of the nocturnal boundary-layer evolution on a slope at the foot of a desert mountain. *J. Appl. Meteor. Climatol.,* **54,** 732–751, doi:10.1175/JAMC-D-14-0223.1.

Leo, L. S., H. J. S. Fernando, and S. Di Sabatino, 2015a: Flow in complex terrain with coastal and urban influence. *J. Environ. Fluid Mech.,* **15,** 349–372, doi:10.1007/s10652-013-9327-y.

Lin, Q., W. R. Lindberg, D. L. Boyer, and H. J. S. Fernando, 1992: Stratified flow past a sphere. *J. Fluid Mech.,* **240,** 315–354, doi:10.1017/S0022112092000119.

Liu, Y., and Coauthors, 2008: The operational mesogamma-scale analysis and forecast system of the U.S. Army Test and Evaluation Command. Part I: Overview of the modeling system, the forecast products, and how the products are used. *J. Appl. Meteor. Climatol.,* **47,** 1077–1092, doi:10.1175/2007JAMC1653.1.

Long, R. R., 1953: Some aspects of the flow of stratified fluids: I. A theoretical investigation. *Tellus,* **5,** 42–58, doi:10.1111/j.2153-3490.1953.tb01035.x.

——, 1972: Finite amplitude disturbances in the flow of inviscid rotating and stratified fluids over obstacles. *Annu. Rev. Fluid Mech.,* **4,** 69–92, doi:10.1146/annurev.fl.04.010172.000441.

Lothon, M., and Coauthors, 2014: The BLLAST field experiment: Boundary-Layer Late Afternoon and Sunset Turbulence. *Atmos. Chem. Phys. Discuss.,* **14,** 10789–10852, doi:10.5194/acpd-14-10789-2014.

Louis, H., 1975: Neugefasstes hohendiagramme der Erde. *Math-Naturwisse Klasse,* B. Messerli B. and J. D. Ives, Eds., Bayerische Akademie der Wissenschaften, 305–326.

Lu, R., and R. P. Turco, 1994: Air pollutant transport in a coastal environment. Part I: Two-dimensional simulations of sea-breeze and mountain effects. *J. Atmos. Sci.,* **51,** 2285–2308, doi:10.1175/1520-0469(1994)051<2285:APTIAC>2.0.CO;2.

Lundquist, K. A., F. K. Chow, and J. K. Lundquist, 2010: An immersed boundary method for the Weather and Research Forecasting model. *Mon. Wea. Rev.,* **138,** 796–817, doi:10.1175/2009MWR2990.1.

——, ——, and ——, 2012: An immersed boundary method enabling large-eddy simulations of complex terrain in the WRF model. *Mon. Wea. Rev.,* **140,** 3936–3955, doi:10.1175/MWR-D-11-00311.1.

Mahrt, L., 1999: Stratified atmospheric boundary layers. *Bound.-Layer Meteor.,* **90,** 375–396, doi:10.1023/A:1001765727956.

Marshall, C. H., K. C. Crawford, K. E. Mitchell, and D. J. Stensrud, 2003: The impact of the land surface physics in the operational NCEP Eta Model on simulating the diurnal cycle: Evaluation and testing using Oklahoma Mesonet data. *Wea. Forecasting,* **18,** 748–768, doi:10.1175/1520-0434(2003)018<0748:TIOTLS>2.0.CO;2.

Mass, C. F., D. Ovens, K. Westrick, and B. A. Colle, 2002: Does increasing horizontal resolution produce more skillful forecasts? The results of two years of real-time numerical weather prediction over the Pacific Northwest. *Bull. Amer. Meteor. Soc.,* **83,** 407–430, doi:10.1175/1520-0477(2002)083<0407:DIHRPM>2.3.CO;2.

Massey, J. D., W. J. Steenburgh, S. W. Hoch, and J. C. Knievel, 2014: Sensitivity of near-surface temperature forecasts to soil properties over a sparsely vegetated dryland region. *J. Appl. Meteor. Climatol.,* **53,** 1976–1995, doi:10.1175/JAMC-D-13-0362.1.

Mayr, G. J., and Coauthors, 2007: Gap flows: Results from the Mesoscale Alpine Programme. *Quart. J. Roy. Meteor. Soc.,* **133,** 881–896, doi:10.1002/qj.66.

McCumber, M. C., and R. A. Pielke, 1981: Simulation of the effects of surface fluxes of heat and moisture in a mesoscale numerical model. *J. Geophys. Res.,* **86,** 9929–9938, doi:10.1029/JC086iC10p09929.

Monti, P., H. J. S. Fernando, M. Princevac, W. C. Chan, T. A. Kowalewski, and E. R. Pardyjak, 2002: Observations of flow and turbulence in the nocturnal boundary layer over a slope. *J. Atmos. Sci.,* **59,** 2513–2534, doi:10.1175/1520-0469(2002)059<2513:OOFATI>2.0.CO;2.

Nadeau, D. F., E. R. Pardyjak, C. W. Higgins, H. J. S. Fernando, and M. B. Parlange, 2011: A simple model for the afternoon and early evening decay of convective turbulence over different land surfaces. *Bound.-Layer Meteor.,* **141,** 301–324, doi:10.1007/s10546-011-9645-x.

——, ——, ——, H. Huwald, and M. B. Parlange, 2013: Flow during the evening transition over steep Alpine slopes. *Quart. J. Roy. Meteor. Soc.,* **139,** 607–624, doi:10.1002/qj.1985.

Ngan, F., H. Kim, P. Lee, B. Dornblaser, and K. Al-Wali, 2013: A study on nocturnal surface wind

speed overprediction by the WRF-ARW model in southeastern Texas. *J. Appl. Meteor. Climatol.,* **52,** 2638–2653, doi:10.1175/JAMC-D-13-060.1.

Pardyjak, E., H. J. S. Fernando, J. C. R. Hunt, A. Grachev, and J. Anderson, 2009: Development of nocturnal flow and transport in a wide open valley. *Meteor. Z.,* **18,** 85–100, doi:10.1127/0941-2948/2009/362.

Politovich, M. K., R. K. Goodrich, C. S. Morse, A. Yates, R. Barron, and S. A. Cohn, 2011: The Juneau terrain-induced turbulence alert system. *Bull. Amer. Meteor. Soc.,* **92,** 299–313, doi:10.1175/2010BAMS3024.1.

Poulos, G. S., J. E. Bossert, T. B. McKee, and R. A. Pielke, 2000: The interaction of katabatic flow and mountain waves. Part I: Observations and idealized simulations. *J. Atmos. Sci.,* **57,** 1919–1936, doi:10.1175/1520-0469(2000)057<1919:TIOKFA>2.0.CO;2.

Prandtl, L., 1942: *Strömungslehre* (*Flow Studies*). Vieweg und Sohn, 382 pp.

Pratt, T., Z. Lin, S. DiSabatino, L. Leo, N. Dodson, and J. Mueller, 2014: Towards estimation of soil moisture using RF polarimetric responses with topographical data and electromagnetic scattering models. *18th Joint Conf. on the Applications of Air Pollution Meteorology with the A&WMA,* Atlanta, GA, Amer. Meteor. Soc., 16.1. [Available online at https://ams.confex.com/ams/94Annual/webprogram/Paper235742.html.]

Price, J. D., and Coauthors, 2011: COLPEX: Field and numerical studies over a region of small hills. *Bull. Amer. Meteor. Soc.,* **92,** 1636–1650, doi:10.1175/2011BAMS3032.1.

Princevac, M., and H. J. S. Fernando, 2008: Morning break-up of cold pools in complex terrain. *J. Fluid Mech.,* **616,** 99–109, doi:10.1017/S0022112008004199.

——, J. C. R. Hunt, and H. J. S. Fernando, 2008: Quasi-steady katabatic winds over long slopes in wide valleys. *J. Atmos. Sci.,* **65,** 627–643, doi:10.1175/2007JAS2110.1.

Pu, Z., H. Zhang, and J. A. Anderson, 2013: Ensemble Kalman filter assimilation of near-surface observations over complex terrain: Comparison with 3DVAR for short-range forecasts. *Tellus,* **65A,** 19620, doi:10.3402/tellusa.v65i0.19620.

——, and Coauthors, 2014: Evaluation of the real-time WRF forecasts during the Mountain Terrain Atmospheric Modeling and Observations (MATERHORN) Program: Performance, comparison with observations, and further implications. *18th Joint Conf. on the Applications of Air Pollution Meteorology with the A&WMA,* Atlanta, GA, Amer. Meteor. Soc., 16.2. [Available online at https://ams.confex.com/ams/94Annual/webprogram/Paper240171.html.]

Queney, P., 1948: The problem of airflow over mountains: A summary of theoretical studies. *Bull. Amer. Meteor. Soc.,* **29,** 16–26.

Rife, D. L., T. T. Warner, F. Chen, and E. G. Astling, 2002: Mechanisms for diurnal boundary layer circulations in the great basin desert. *Mon. Wea. Rev.,* **130,** 921–938, doi:10.1175/1520-0493(2002)130<0921:MFDBLC>2.0.CO;2.

Rotach, M. W., and D. Zardi, 2007: On the boundary-layer structure over highly complex terrain: Key findings from MAP. *Quart. J. Roy. Meteor. Soc.,* **133,** 937–948, doi:10.1002/qj.71.

Smedman, A.-S., U. Högström, J. C. R. Hunt, and E. Sahlée, 2007: Heat/mass transfer in the slightly unstable atmospheric surface layer. *Quart. J. Roy. Meteor. Soc.,* **133,** 37–51, doi:10.1002/qj.7.

Snyder, W. H., and Coauthors, 1985: The structure of strongly stratified flow over hills: Dividing-streamline concept. *J. Fluid Mech.,* **152,** 249–288, doi:10.1017/S0022112085000684.

Soil Survey Staff, 2014: Web soil survey. Natural Resources Conservation Service, United States Department of Agriculture, accessed 28 May 2014. [Available online at http://websoilsurvey.nrcs.usda.gov/.]

Steenburgh, W. J., C. R. Neuman, G. L. West, and L. F. Bosart, 2009: Discrete frontal propagation over the Sierra-Cascade Mountains and Intermountain West. *Mon. Wea. Rev.,* **137,** 2000–2020, doi:10.1175/2008MWR2811.1.

Strobach, K., 1991: *Unser Planet Erde: Ursprung und Dynamik.* Gebruder Bornträger, 253 pp.

Taylor, P. A., P. J. Mason, and E. F. Bradley, 1987: Boundary-layer flow over low hills. *Bound.-Layer Meteor.,* **39** (1–2), 107–132, doi:10.1007/BF00121870.

Thomas, C. K., A. M. Kennedy, J. S. Selker, A. Moretti, M. H. Schroth, A. R. Smoot, N. B. Tufillaro, and M. J. Zeeman, 2012: High-resolution fibre-optic temperature sensing: A new tool to study the two-dimensional structure of atmospheric surface layer flow. *Bound.-Layer Meteor.,* **142,** 177–192, doi:10.1007/s10546-011-9672-7.

West, G. L., and W. J. Steenburgh, 2010: Life cycle and mesoscale frontal structure of an intermountain cyclone. *Mon. Wea. Rev.,* **138,** 2528–2545, doi:10.1175/2010MWR3274.1.

——, and ——, 2011: Influences of the Sierra Nevada on intermountain cold-front evolution. *Mon. Wea. Rev.,* **139,** 3184–3207, doi:10.1175/MWR-D-10-05076.1.

Whiteman, C. D., 1982: Breakup of temperature inversions in deep mountain valleys: Part I. Observations. *J. Appl. Meteor.,* **21,** 270–289, doi:10.1175/1520-0450(1982)021<0270:BOTIID>2.0.CO;2.

——, 2000: *Mountain Meteorology: Fundamentals and Applications.* Oxford University Press, 355 pp.

——, and Coauthors, 2008: METCRAX 2006: Meteorological experiment in Arizona's Meteor Crater. *Bull. Amer. Meteor. Soc.,* **89,** 1665–1680, doi:10.1175/2008BAMS2574.1.

Wile, S. M., J. P. Hacker, and K. H. Chilcoat, 2015: The potential utility of high-resolution ensemble sensitivities during weak flow in complex terrain. *Wea. Forecasting,* in press.

Winters, H. A., G. A. Galloway Jr., W. J. Reynolds, and D. W. Rhyne, 2001: *Battling the Elements: Weather and Terrain in the Conduct of War.* The Johns Hopkins University Press, 226 pp.

Wood, N., 2000: Wind flow over complex terrain: A historical perspective and prospect for large-eddy modeling. *Bound.-Layer Meteor.,* **96,** 11–32, doi:10.1023/A:1002017732694.

WRCC, 2014: Western historical climate summaries. Western Regional Climate Center, accessed 15 Sep 2015. [Available online at www.wrcc.dri.edu/Climsum.html.]

Zardi, D., and C. D. Whiteman, 2013: Diurnal mountain wind systems. *Mountain Weather Research and Forecasting,* F. K. Chow, S. F. J. De Wekker, and B. Snyder, Eds., Springer, 35–119.

Zhang, H., and Z. Pu, 2014: Predictability of atmospheric conditions over complex terrain with ensemble Kalman filter data assimilation: Evaluation with observations from MATERHORN field program. *18th Joint Conf. on the Applications of Air Pollution Meteorology with the A&WMA,* Atlanta, GA, Amer. Meteor. Soc., 16.5. [Available online at https://ams.confex.com/ams/94Annual/webprogram/Paper240176.html.]

——, Z. Pu, and X. Zhang, 2013: Examination of errors in near-surface temperature and wind from WRF numerical simulations in regions of complex terrain. *Wea. Forecasting,* **28,** 893–914, doi:10.1175/WAF-D-12-00109.1.